



TECHNISCHE
UNIVERSITÄT
WIEN

DIPLOMARBEIT

DMFT on the real frequency axis using exact diagonalization and restricted active space

zur Erlangung des akademischen Grades
Diplom-Ingenieur

im Rahmen des Studiums
Physikalische Energie- und Messtechnik

eingereicht von
Frank Takara Ebel
Matrikelnummer 01429282

ausgeführt am Institut für Festkörperphysik
der Fakultät für Physik der Technischen Universität Wien

Betreuung

Betreuer: Univ.-Prof. Dr. Karsten Held

Mitwirkung: Dr. Martin Braß

Mitwirkung: Dr. Markus Wallerberger

Wien, 2025-12-11

Frank Ebel

Karsten Held



Die approbierte gedruckte Originalversion dieser Diplomarbeit ist an der TU Wien Bibliothek verfügbar
The approved original version of this thesis is available in print at TU Wien Bibliothek.

Abstract

In this thesis we present an impurity solver for dynamical mean-field theory. The use of a restricted active basis set allows us to couple the impurity to hundreds of bath sites at polynomial cost. Dynamical quantities are computed directly on the real axis without the introduction of any broadening. In contrast to most previous works the self-energy is calculated using a symmetric improved estimator by combining four correlators and its imaginary part is negative by construction. We study the Mott metal-to-insulator transition on the Bethe lattice at zero temperature and observe sharp features at the inner edge of the Hubbard bands. The quasiparticle weight and impurity double occupation are compared against results of numerical renormalization group calculations.



Die approbierte gedruckte Originalversion dieser Diplomarbeit ist an der TU Wien Bibliothek verfügbar
The approved original version of this thesis is available in print at TU Wien Bibliothek.

Kurzfassung

In dieser Arbeit präsentieren wir einen Algorithmus zur Lösung des Anderson Störstellenproblems für die dynamische Molekularfeldtheorie. Durch den Gebrauch eines eingeschränkten Hilbertraums kann diese Störstelle in polynomialer Rechenzeit an hunderte Badgitterplätze gekoppelt werden. Dynamische Größen werden direkt an der reellen Achse ohne Verbreiterung berechnet. Im Gegensatz zu vielen vorigen Arbeiten wird die Selbstenergie durch einem symmetrisch verbesserten Schätzer mittels vier Korrelatoren berechnet und ihr Imaginärteil ist per Konstruktion negativ. Wir analysieren den Mott Übergang von einem Metall zu Isolator auf dem Bethe Gitter am absoluten Temperaturnullpunkt und beobachten zusätzliche feine Strukturen auf den inneren Seiten der Hubbardbänder. Das Gewicht des Quasiteilchen und die Doppelbesetzung der Störstelle werden gegen Resultate der numerische Renormierungsgruppe verglichen.



Die approbierte gedruckte Originalversion dieser Diplomarbeit ist an der TU Wien Bibliothek verfügbar
The approved original version of this thesis is available in print at TU Wien Bibliothek.

Contents

1. Introduction	9
1.1. Outline	9
2. Models and formalism	11
2.1. Bethe lattice	11
2.2. Hubbard model	12
2.3. Anderson impurity model	13
2.4. Green's function and correlators	14
2.4.1. Spectral function	15
2.4.2. Moments	17
2.5. Self-energy	17
2.6. DMFT	19
3. Numerical methods	21
3.1. Natural impurity orbitals and restricted active space	22
3.2. Lanczos algorithm	24
3.2.1. Block variant	25
3.3. Ground state	26
3.4. Correlator representation	26
3.4.1. Broadening	28
3.5. Self-energy calculation	29
4. Results	31
4.1. Ground state convergence	32
4.2. Performance analysis	33
4.3. Correlators	35
4.4. Spectral function	36
4.5. Self-energy	38
4.6. Mott transition	40
4.7. CeRu_4Sn_6	43
5. Conclusion and outlook	45
A. Derivations	47
A.1. Fourier transform of the retarded correlator	47
A.2. DMFT simplification	48
A.3. Shifting of poles	49
A.4. Number of Slater determinants	49

Contents

B. Code Tutorial	53
B.1. Non-interacting Bethe lattice in infinite dimensions	53
B.2. DMFT step	56
B.2.1. Impurity	56
B.2.2. Hybridization function	56
B.2.3. Ground state	57
B.2.4. Block correlator	57
B.2.5. Self-energy	58
B.2.6. Update hybridization	59

1. Introduction

In strongly correlated materials the interplay between electrons driven by the Coulomb interaction can give rise to interesting phenomena, e.g., Kondo physics in heavy fermions [1, 2], the Mott metal-to-insulator transition [3, 4], and many more [5]. A popular method to study these materials is dynamical mean-field theory (DMFT) [6–8] which maps a system of interacting electrons on a lattice to a system where electronic interactions are only present at an impurity that is coupled to a non-interacting bath. Many approaches exist to solve this model, including quantum Monte Carlo (QMC) [9–12], Wilson’s numerical renormalization group (NRG) [13–16], and exact diagonalization (ED) [17–21], with advantages and disadvantages between all of them. A strong argument for QMC is the fact that it can easily be extended to impurities containing multiple orbitals which is often necessary to describe realistic materials. However, the problem is that sampling is done on the imaginary axis which requires analytic continuation to obtain real frequency data, which is an ill-conditioned inversion [22–24]. In contrast, NRG — which is designed for impurity problems — gives quantities on the real axis, has excellent resolution for small frequencies but suffers at larger ones due to logarithmic discretization [16]. ED methods can be applied very broadly, obtain quantities on the real axis as well but suffer from discretization artifacts. Continuous quantities need to be discretized to a few poles to keep the exponentially growing many-body Hilbert space manageable. In [20, 21] it was shown how to counter this exponential increase in complexity by finding an optimized one-particle basis in combination with a restricted active space (RAS). However, due to discretization, the self-energy contained non-physical values. In this work we combine their approach together with the symmetric improved estimator for the self-energy introduced for NRG [25] and also used for QMC [26]. This allows us to obtain physical self-energies even for a discrete bath. In contrast to NRG, we introduce no broadening and calculate it directly on the real axis. With this approach we study the Mott metal-to-insulator transition on the half-filled $z \rightarrow \infty$ Bethe lattice.

1.1. Outline

The thesis is organized as follows: In [Ch. 2](#) we describe the necessary model and formalism for this work. We start by introducing the Bethe lattice and the limit of infinite dimensions. Afterward we create model Hamiltonians to describe interacting electrons, introduce the Green’s function formalism and the self-energy. Finally, we explain DMFT and arrive at a set of equations which need to be solved self-consistently. In [Ch. 3](#) we describe the numerical methods used to develop our code.

1. Introduction

We explain the natural impurity orbitals [20, 21] and the RAS approach, allowing us to solve our system in polynomial instead of exponential time. This is followed by the introduction of the Lanczos algorithm and representation of complex functions as a sum of discrete poles. [Ch. 4](#) focuses on the results of our work. Finally, we summarize and discuss possible enhancements in [Ch. 5](#).

2. Models and formalism

2.1. Bethe lattice

In solid-states physics we study crystals in which atoms are periodically arranged on a Bravais lattice. Given a set of basis vectors $\{\mathbf{a}_i\}$, the lattice is periodic for all translations

$$\mathbf{R} = \sum_i n_i \mathbf{a}_i \quad (2.1)$$

for any integer $n_i \in \mathbb{Z}$.

In this work however, we look at the Bethe lattice which is only characterized by a single quantity: the coordination number z . It is an infinite graph where each vertex is connected to z neighbors¹. A sketch for $z = 3$ is given in Fig. 2.1(a): We choose the black vertex in the center as the root node. It is connected to three nodes

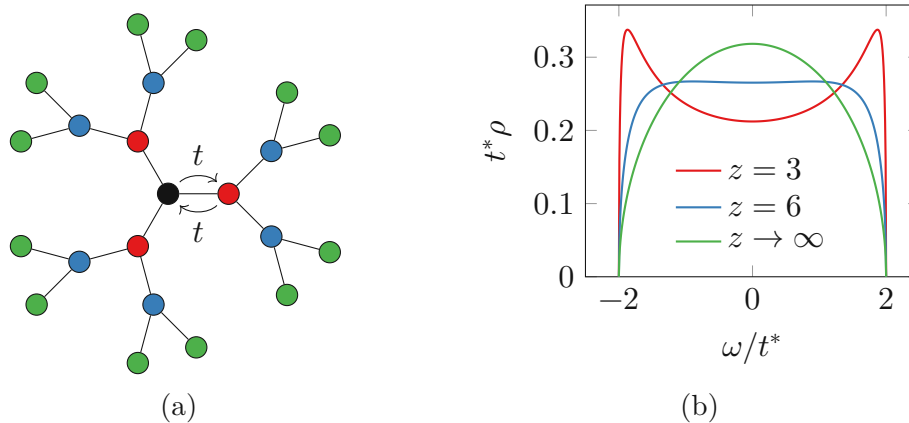


Figure 2.1.: (a) Bethe lattice with coordination number $z = 3$ and hopping amplitude t . (b) Density of states for different connectivities z with hopping set to unity $t^* = 1$ (adapted from [11]).

(marked in red) which in turn are also connected to three nodes (each red node is connected to the original black node and two blue nodes). This scheme is then infinitely repeated for each site.

We can then model electron movement as hopping from a given site to one of the z neighbors. If we assume that hopping to each nearest neighbor is equally likely and assign it the probability p^* , the total probability of movement is zp^* . In the limit of

¹It is a lattice in the sense that a translation shifts the root node which is set arbitrarily in contrast to the Bravais lattice which is constructed by tiling cells characterized by basis vectors.

2. Models and formalism

infinite connectivity $z \rightarrow \infty$ (infinite dimensions) this will diverge, necessitating a renormalization. Thus, the rescaled probability is set to $p = p^*/z$ such that the total probability zp stays finite. Instead of working with a hopping probability, we instead introduce the hopping amplitude $t = t^*/\sqrt{z}$ [8]. Such a hopping process between neighboring sites is sketched in Fig. 2.1(a).

For the Bethe lattice, the density of states² (DOS) for $z \rightarrow \infty$ reads [30]

$$\rho(\omega) = \frac{1}{2\pi t^{*2}} \sqrt{4t^{*2} - \omega^2} \quad (2.2)$$

which is shown in Fig. 2.1(b). We can define the bandwidth $W = 4t^*$ as the difference between the highest and lowest frequency where this expression vanishes. This relation can be rewritten by using the half-bandwidth $D = W/2$ instead:

$$\rho(\omega) = \frac{2}{\pi D^2} \sqrt{D^2 - \omega^2}. \quad (2.3)$$

2.2. Hubbard model

Although we do not explicitly calculate properties of the system through the Hubbard model directly³ [31], we nevertheless want to mention it briefly due to its importance in DMFT. Denoting the electron creation operator of site i and spin $\sigma \in \{\uparrow, \downarrow\}$ as $d_{i\sigma}^\dagger$ and respective annihilator as $d_{i\sigma}$ its Hamiltonian⁴ reads

$$H = -t \sum_{\langle ij \rangle \sigma} (d_{i\sigma}^\dagger d_{j\sigma} + d_{j\sigma}^\dagger d_{i\sigma}) + U \sum_i n_{i\uparrow} n_{i\downarrow} + (\epsilon - \mu) \sum_{i\sigma} n_{i\sigma}, \quad (2.4)$$

with a sketch given in Fig. 2.2. Each site can be occupied by up to two electrons. The first term describes the kinetics of the system: Electrons can hop between nearest-neighbors $\langle ij \rangle$ with the hopping amplitude t . If two electrons are on the same site, they are repulsed by the local Coulomb interaction U expressed by the second term (occupation $n_{i\sigma} = d_{i\sigma}^\dagger d_{i\sigma}$). The last term describes the on-site energy ϵ and chemical potential μ which control the average occupation per site. In this work we look at the half-filled system $\epsilon = 0$, $\mu = U/2$ with average occupation $\langle n \rangle = 1$.

Although the model Hamiltonian looks simple at first glance, no analytical solution exists for the general case. The problem is that the kinetic part is diagonal in momentum space, while the Coulomb interaction is diagonal in real space.

²This distribution is also known as the Wigner semicircle distribution which is the eigenvalue distribution of random matrices [27, 28]. They are related to the DOS in as much as a random walk on the Bethe lattice. As the graph has no closed loops, a particle must necessarily take the same path back to return to its origin [29].

³We only obtain quantities in the DMFT approximation which is exact for infinite dimensions.

⁴In this work we look at the SU(2) symmetric model which means that quantities (e.g., on-site energies) are spin-independent. Thus, we omit the spin index.

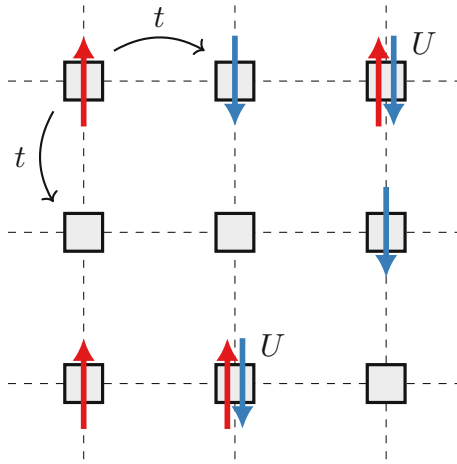


Figure 2.2.: Hubbard model for a 2D square lattice. The hopping amplitude between neighboring sites is given by t and U describes the Coulomb repulsion on a doubly occupied site.

2.3. Anderson impurity model

Instead of having a repulsion U on each site, we can create a model in which only one site is correlated (called *impurity site* or just *impurity*) and embedded in a non-interacting bath. This is called the Anderson impurity model [32] and its Hamiltonian can be written as

$$H = H_{\text{imp}} + H_{\text{bath}} + H_{\text{imp-bath}}. \quad (2.5)$$

The impurity can be further split into a non-interacting and interacting part using the occupation operator $n_{\sigma} = d_{\sigma}^{\dagger} d_{\sigma}$

$$H_{\text{imp},0} = (\epsilon - \mu) \sum_{\sigma} n_{\sigma} \quad (2.6)$$

$$H_{\text{int}} = U n_{\uparrow} n_{\downarrow}, \quad (2.7)$$

which has the same structure as Eq. (2.4) but only for a single site. For the bath we define the annihilator $b_{k\sigma}$ and energy ϵ_k , allowing us to write

$$H_{\text{bath}} = \sum_{k\sigma} \epsilon_k b_{k\sigma}^{\dagger} b_{k\sigma}. \quad (2.8)$$

Finally, the interaction between impurity and bath is given by the hybridization strength V_k :

$$H_{\text{imp-bath}} = \sum_{k\sigma} V_k d_{\sigma}^{\dagger} b_{k\sigma} + V_k^* b_{k\sigma}^{\dagger} d_{\sigma}. \quad (2.9)$$

A graphical representation of the Hamiltonian in Eq. (2.5) is given in Fig. 2.3: each bath site has a given filling and electrons from each bath site can hop in and out of the impurity. The last two terms of Eq. (2.5) are commonly combined into the *hybridization function*

$$\Delta(\omega) = \sum_k \frac{|V_k|^2}{\omega + i0^+ - \epsilon_k}. \quad (2.10)$$

2. Models and formalism

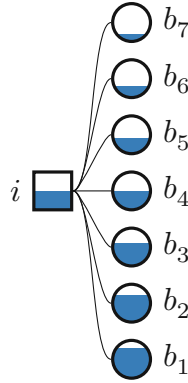


Figure 2.3.: Sketch of an Anderson impurity model. Impurity (square) interacting with bath sites (circles). Site occupation is indicated by fill level, where a full site corresponds to one double occupation. Furthermore, hopping between the impurity and bath sites is shown by lines (adapted from [21]).

This function describes the dynamics of the bath, i.e., how electrons of a given energy can hop in and out of the impurity. It is introduced here, as it will be important in DMFT (Sec. 2.6).

2.4. Green's function and correlators

The retarded Green's function is defined as [33]

$$G(t) = -i\Theta(t)\langle\{d_{i\sigma}(t), d_{i\sigma}^\dagger\}\rangle, \quad (2.11)$$

with the step function Θ and anticommutator $\{\cdot, \cdot\}$. In the Heisenberg picture⁵ the time evolution of the annihilation operator is given as $d_{i\sigma}(t) = e^{iHt}d_{i\sigma}e^{-iHt}$. At zero temperature $T = 0$, the expectation value is evaluated with respect to the ground state $\langle \cdot \rangle = \langle \psi_0 | \cdot | \psi_0 \rangle$ only. Because of the anticommutator, this function consists of two terms which can be interpreted as the propagation of a particle or hole respectively, e.g., at time 0 a particle is added at site i with spin σ to the ground state. The system then evolves as dictated by the Hamiltonian. At a later time t the particle is removed from the same site and the resulting state is then projected onto the initial state. The local Green's function (for equal sites i) can therefore be interpreted as the probability amplitude of a particle returning to its origin at time t [33].

This method can be generalized for two arbitrary fermionic operators A, B defining a *correlation function* or just *correlator*

$$C(t) = -i\Theta(t)\langle\{A(t), B\}\rangle. \quad (2.12)$$

⁵In this work we look at time-independent Hamiltonians. Thus, we can set our time origin arbitrarily and our time evolution operator is given as $U(t, 0) = e^{-iHt}$ which evolves the system from 0 to t . Otherwise, one needs to use a general time evolution $U(t, t_0)$ based on the time-dependent Schrödinger equation.

Following the notation of [14, 25], we will denote the Fourier transform⁶ of Eq. (2.12) as

$$C_\omega := \lim_{\delta \rightarrow 0^+} \int_{-\infty}^{\infty} dt e^{i(\omega+i\delta)t} C(t) =: \langle\langle A, B \rangle\rangle_\omega. \quad (2.13)$$

From this point onwards, we will write function arguments or variables as subscripts, e.g., $C(\omega) \rightarrow C_\omega$ to keep notation compact. As Eq. (2.12) contains two terms (from the anticommutator) and the Fourier transform is linear, $C_\omega = C_\omega^+ + C_\omega^-$ can be combined from partial correlators with poles on the positive and negative real axis, respectively. Given the ground state energy E_0 , they are written as

$$C_\omega^+ = \left\langle A \frac{1}{\omega + i0^+ - (H - E_0)} B \right\rangle, \quad (2.14a)$$

$$C_\omega^- = \left\langle B \frac{1}{\omega + i0^+ + (H - E_0)} A \right\rangle. \quad (2.14b)$$

A detailed derivation is available in App. A.1. As we are only interested in energies relative to the ground state, we can absorb it into our Hamiltonian

$$H \rightarrow H - E_0 \quad (2.15)$$

such that all eigenvalues are non-negative: $H|n\rangle = E_n|n\rangle$ with $E_n \geq 0$. Given such a full decomposition of H allows us to write Eq. (2.14) in the so-called *Lehmann representation*

$$C_\omega^+ = \sum_n \frac{\langle \psi_0 | A | n \rangle \langle n | B | \psi_0 \rangle}{\omega + i0^+ - E_n}, \quad (2.16a)$$

$$C_\omega^- = \sum_n \frac{\langle \psi_0 | B | n \rangle \langle n | A | \psi_0 \rangle}{\omega + i0^+ - E_n}. \quad (2.16b)$$

We define *diagonal correlators* as those where $A = B^\dagger$, e.g., our local Green's function. For these, the numerators of Eq. (2.16) simplify to positive real values

$$\langle \psi_0 | A | n \rangle \langle n | B | \psi_0 \rangle = |\langle n | A^\dagger | \psi_0 \rangle|^2, \quad (2.17a)$$

$$\langle \psi_0 | B | n \rangle \langle n | A | \psi_0 \rangle = |\langle n | A | \psi_0 \rangle|^2. \quad (2.17b)$$

2.4.1. Spectral function

Given our Green's function, we can split it up into a real and imaginary part. Taking the latter and rescaling it allows us to define the spectral function

$$A_\omega := -\frac{1}{\pi} \text{Im } G_\omega, \quad (2.18)$$

⁶As our Hamiltonian is hermitian, its eigenvalues (poles) lie on the real axis. This means that the correlator is analytic in the upper and lower complex plane and allows us to approach it from above the real axis $\omega + i0^+$ (positive times $\Theta(t)$) which is called the retarded Green's function. If one comes from below the real axis $\omega - i0^+$ (negative times $\Theta(-t)$), it is called the advanced Green's function. Using different approaches for $\omega \gtrless 0$ gives rise to the so-called causal and anti-causal correlator.

2. Models and formalism

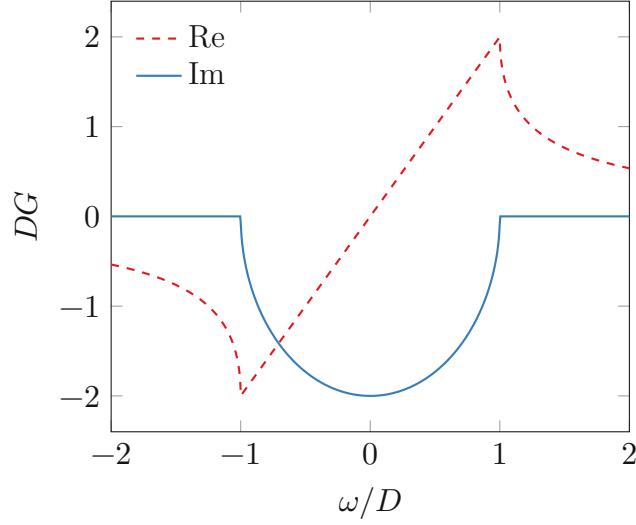


Figure 2.4.: Real and imaginary part of the non-interacting Green's function of the Bethe lattice in infinite dimensions in units of the half-bandwidth D .

which can be generalized to the *spectral part* of C

$$A_\omega := -\frac{1}{\pi} \text{Im} C_\omega. \quad (2.19)$$

As our correlator is analytic in the upper complex plane, the real and imaginary part are not independent but related by Kramers-Kronig transformations (Hilbert transform) [33]

$$\text{Re} C_\omega = -\frac{1}{\pi} \mathcal{P} \int_{-\infty}^{\infty} d\omega' \frac{\text{Im} C_{\omega'}}{\omega - \omega'}, \quad (2.20a)$$

$$\text{Im} C_\omega = \frac{1}{\pi} \mathcal{P} \int_{-\infty}^{\infty} d\omega' \frac{\text{Re} C_{\omega'}}{\omega - \omega'}, \quad (2.20b)$$

with \mathcal{P} denoting the Cauchy principal value integral. Thus, using our non-interacting density of the Bethe lattice (Eq. (2.3)) as a spectrum, we can calculate the corresponding real part. This allows us to create a non-interacting Green's function [33] (labeled with a subscript 0)

$$G_{0,\omega} = \frac{2}{D^2} \left(\omega - \text{sgn}(\omega) \sqrt{\omega^2 - D^2} \right), \quad (2.21)$$

which is shown in Fig. 2.4. The signum function at zero is defined as $\text{sgn}(0^\pm) = \pm 1$. As the complex square root has a branch cut, the imaginary part is taken to be positive.

For the Bethe lattice, its hybridization function is just a rescaled Green's function [7]

$$\Delta_\omega = \frac{D^2}{4} G_\omega. \quad (2.22)$$

2.4.2. Moments

The moments of a correlator [20, 25, 34] are defined as

$$C^{(n)} = -\frac{1}{\pi} \int_{-\infty}^{\infty} d\omega \omega^n \text{Im} C_{\omega} = \int_{-\infty}^{\infty} d\omega \omega^n A_{\omega}, \quad (2.23)$$

allowing us to write C_{ω} in a high-frequency expansion [34]

$$C_{\omega} = \sum_{n=0}^{\infty} \frac{C^{(n)}}{\omega^{n+1}}. \quad (2.24)$$

An alternative but equivalent approach is to use the Heisenberg equation of motion. We define $\mathcal{L}A = [A, H]$ as the commutator of an operator A with the Hamiltonian which allows us to formulate the moments as [34]

$$C^{(n)} = \langle \{ \mathcal{L}^n A, B \} \rangle, \quad (2.25)$$

e.g., $G^{(0)} = \langle \{ d_{i\sigma}, d_{i\sigma}^{\dagger} \} \rangle = 1$ by definition of anticommutative rules for fermionic operators. For the particle-hole symmetric system on the Bethe lattice the first four moments of the Green's function are [34]

$$G^{(0)} = 1, \quad (2.26a)$$

$$G^{(1)} = 0, \quad (2.26b)$$

$$G^{(2)} = \frac{U^2}{4} + \frac{D^2}{4}, \quad (2.26c)$$

$$G^{(3)} = 0. \quad (2.26d)$$

Due to symmetry $A_{-\omega} = A_{\omega}$ for the half-filled spectrum, all odd moments vanish.

2.5. Self-energy

As mentioned in the previous section, the Green's function G_{ω} describes the propagation of an electron/hole in our system. The quantity that connects these between an interacting and non-interacting system is the so-called *self-energy* defined by the Dyson equation⁷ [33]

$$\Sigma_{\omega} = (G_{0,\omega})^{-1} - (G_{\omega})^{-1}. \quad (2.27)$$

We can define the moments of the self-energy in the same way as correlators in Sec. 2.4.2, to write down a high-energy expansion [34]

$$\Sigma_{\omega} = \sum_{n=-1}^{\infty} \frac{\Sigma^{(n)}}{\omega^{n+1}}. \quad (2.28)$$

⁷This relation can be motivated by Feynman diagrams.

2. Models and formalism

In contrast to Eq. (2.24), the self-energy contains a constant (frequency independent) term which is called the Hartree term Σ^{H} . The analytic moments for half-filling are [34]

$$\Sigma^{\text{H}} = \frac{U}{2}, \quad (2.29\text{a})$$

$$\Sigma^{(0)} = \frac{U^4}{4}, \quad (2.29\text{b})$$

$$\Sigma^{(1)} = 0, \quad (2.29\text{c})$$

with every odd moment vanishing.

Although the Dyson equation is exact, it poses an issue [14]: $G_{0,\omega}$ is known analytically while G_ω can only be obtained numerically most of the time. Thus, calculating the difference as dictated by Eq. (2.27) is prone to catastrophic cancellation if the difference becomes very small⁸. To mitigate this, Bulla et al. [14] calculated the self-energy using a quotient of two correlators. In this work we go a step further by using the symmetric improved estimator [26] introduced by Kugler [25] which will be summarized in the following. We introduce the auxiliary operator

$$q_\sigma = [d_\sigma, H_{\text{int}}] = U d_\sigma n_{-\sigma} \quad (2.30)$$

with the interacting Hamiltonian from Eq. (2.7). Here, $-\sigma$ indicates opposite spin. This allows us to calculate the Hartree term directly

$$\Sigma^{\text{H}} = \langle \{q_\sigma^\dagger, d_\sigma\} \rangle. \quad (2.31)$$

We then employ a shift⁹

$$\tilde{q}_\sigma = q_\sigma - \Sigma^{\text{H}} d_\sigma \quad (2.32)$$

and obtain four correlation functions

$$I_\omega = \langle \langle \tilde{q}_\sigma, \tilde{q}_\sigma^\dagger \rangle \rangle_\omega, \quad F_\omega^{\text{L}} = \langle \langle \tilde{q}_\sigma, d_\sigma^\dagger \rangle \rangle_\omega, \quad (2.33\text{a})$$

$$F_\omega^{\text{R}} = \langle \langle d_\sigma, \tilde{q}_\sigma^\dagger \rangle \rangle_\omega, \quad G_\omega = \langle \langle d_\sigma, d_\sigma^\dagger \rangle \rangle_\omega, \quad (2.33\text{b})$$

The self-energy is computed as

$$\Sigma_\omega^{\text{IFG}} = \Sigma^{\text{H}} + I_\omega - F_\omega^{\text{L}} (G_\omega)^{-1} F_\omega^{\text{R}}. \quad (2.34)$$

⁸This happens around the Fermi level which is the most important region.

⁹As noted by Kugler, this is especially convenient for particle-hole symmetric systems. Strictly speaking this shift is not necessary, but it will simplify our calculation as it will create a diagonal matrix in Eq. (3.43).

2.6. DMFT

As mentioned in [Sec. 2.2](#), the Hubbard model has no analytical solution in arbitrary dimensions d . In the limit $d \rightarrow \infty$ however, it can be solved by dynamical mean-field theory (DMFT) [7], which takes a single lattice site as a representative and averages all spacial fluctuations around it, only keeping time correlations (hence the term *dynamical mean-field*).

A given Hubbard Hamiltonian is solved¹⁰ by a self-consistency loop, which repeatedly maps between the Hubbard model and Anderson impurity model until their Green's function coincide. Let us briefly recapitulate this DMFT self-consistency loop, for further details see [7, 8]: Given a Hubbard Hamiltonian, we can define its local Green's function

$$G_{\text{loc},\omega} = \frac{1}{V_{\text{BZ}}} \int_{\text{BZ}} d\mathbf{k} G_{\mathbf{k}\omega} \quad (2.35)$$

by averaging over the Brillouin zone BZ. In DMFT, this is approximated by assuming that the self-energy is purely local ($\Sigma_{\mathbf{k}\omega} \rightarrow \Sigma_{\omega}$)

$$G_{\text{loc},\omega} \approx \frac{1}{V_{\text{BZ}}} \int_{\text{BZ}} d\mathbf{k} \frac{1}{\omega + i0^+ + \mu - \epsilon_{\mathbf{k}} - \Sigma_{\omega}}. \quad (2.36)$$

We then enforce that this Green's function coincides with the impurity Green's function of the corresponding Anderson impurity model: $G_{\text{loc},\omega} \equiv \mathcal{G}_{\omega}$.

Rearranging the Dyson equation ([Eq. \(2.27\)](#)) for the impurity then gives us the non-interacting impurity Green's function of this Anderson impurity model

$$(\mathcal{G}_{0,\omega})^{-1} = (G_{\text{loc},\omega})^{-1} + \Sigma_{\omega} \quad (2.37)$$

$$= \omega + i0^+ + \mu - \epsilon - \Delta_{\omega}, \quad (2.38)$$

which is rewritten into terms, containing the impurity energy $\epsilon - \mu$ and hybridization function Δ_{ω} . Given these terms, we can write down a non-interacting Hamiltonian of [Eq. \(2.5\)](#) which leads to the given Green's function $\mathcal{G}_{0,\omega}$. After adding the interacting term of [Eq. \(2.7\)](#), we can solve the impurity Hamiltonian yielding us a new impurity Green's function \mathcal{G}_{ω} and self-energy Σ_{ω} . Subsequently, we use this impurity self-energy to calculate a new lattice Green's function using [Eq. \(2.36\)](#), closing our self-consistency loop. These steps are repeated until the calculated impurity Green's function equals the local lattice Green's function $\mathcal{G}_{\omega} \equiv G_{\text{loc},\omega}$.

For the special case of a lattice in infinite dimensions, one can skip the calculation of the lattice Green's function and directly update the hybridization [20]:

$$\Delta(\omega) = \Delta_0(\omega + \mu - \mu_0 - \Sigma_{\omega}), \quad (2.39)$$

with a derivation given in [App. A.2](#).

¹⁰Strictly speaking we do not need to solve the Hamiltonian but find the corresponding interacting Green's function.



Die approbierte gedruckte Originalversion dieser Diplomarbeit ist an der TU Wien Bibliothek verfügbar
The approved original version of this thesis is available in print at TU Wien Bibliothek.

3. Numerical methods

The goal of this chapter is to explain the numerical implementation of our impurity solver and subsequent DMFT self-consistency loop. Most ideas are taken from [20, 21, 25, 35].

The main problem in quantum many-body physics is the size of the associated Hilbert space [36]. In principle there are infinitely many states an electron can occupy. One method to calculate models on a computer is therefore to discretize the space by choosing a finite number $i \in \{1, \dots, n\}$ of one-particle wave functions $\{|\phi_i\rangle\}$ with energies $\{\epsilon_i\}$. A simple discretization of the semicircular DOS (Eq. (2.3)) is shown in Fig. 3.1. Using this basis, we can combine the one-particle wave functions

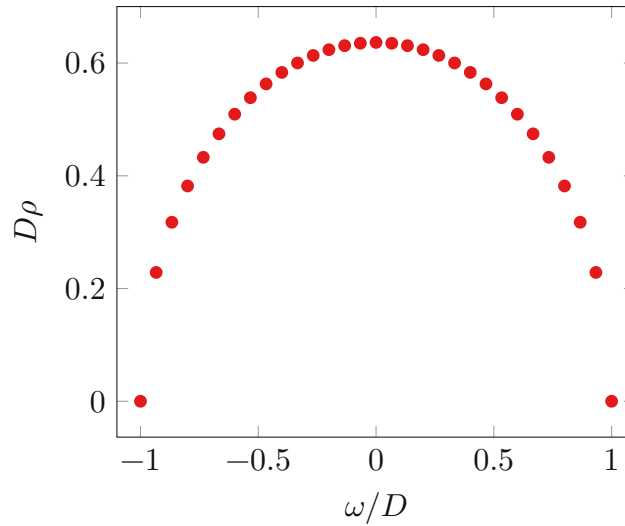


Figure 3.1.: Possible discretization of the semicircular DOS (Eq. (2.3)) with half-bandwidth D to 31 orbitals.

to Slater determinants¹

$$|\alpha\rangle = \prod_{i\sigma} (c_{i\sigma}^\dagger)^{n_{i\sigma}} |0\rangle, \quad n_{i\sigma} \in \{0, 1\}, \quad (3.1)$$

which allows us to write wave functions as linear combinations of all possible configurations $\{n_{i\sigma}\}$.

$$|\psi\rangle = \sum_j \alpha_j |\alpha_j\rangle. \quad (3.2)$$

¹Formally we must distinguish between the occupation number operator $n_{i\sigma} = c_{i\sigma}^\dagger c_{i\sigma}$ and occupation number $n_{i\sigma} \in \{0, 1\}$ which is why sometimes the former is written with a hat $\hat{n}_{i\sigma}$ in the literature. In this work this was not done to avoid visual clutter and the meaning can be inferred from context.

3. Numerical methods

As each site has four possible states² the dimension of the Hilbert space (number of possible Slater determinants) grows as 4^n limiting exact diagonalization (ED) to $O(10)$ sites. To further reduce the dimensionality of our space, we can make use of symmetries, which allow us to decompose the Hilbert space into subspaces that are invariant under certain operations and characterized by conserved quantum numbers [37]. The Hamiltonian thus becomes block-diagonal with respect to these subspaces. One example is the number operator $N = \sum_{i\sigma} c_{i\sigma}^\dagger c_{i\sigma}$: If our Hamiltonian conserves it, $[H, N] = 0$, we know that H and N share a common basis. Thus, we can decompose our Hamiltonian into blocks of $p \in \{0, \dots, 2n\}$ particles where the dimensionality of each block is given by

$$\binom{2n}{p}. \quad (3.3)$$

As our Hamiltonian is $SU(2)$ symmetric, we can split it further into blocks of fixed N_\uparrow and N_\downarrow reducing the dimensionality to

$$\binom{n}{p_\uparrow} \binom{n}{p_\downarrow}. \quad (3.4)$$

For the half-filled block where $p_\sigma = n/2$ its asymptotic behavior is

$$\binom{n}{n/2} \binom{n}{n/2} \approx \frac{2}{\pi} \frac{4^n}{n}, \quad (3.5)$$

which for $n = 140$ sites is approximately $9 \cdot 10^{81}$ exceeding the number of protons in the observable universe $O(10^{80})$. The total spin S^2 is a further conserved quantity. However, it is cumbersome to utilize it; and therefore many exact diagonalization algorithms do not employ this symmetry.

3.1. Natural impurity orbitals and restricted active space

To mitigate this issue, we take the same approach as [21]. Instead of exploring the full Hilbert space of n bath sites in an Anderson impurity model, we consider only a very small subset.

In the first step, the one particle basis $\{|\phi_i\rangle\}$ is optimized to the so-called *natural impurity orbitals* which — compared to the commonly used *natural orbitals* in quantum chemistry — optimize only the bath basis while keeping the impurity unchanged³. This new geometry is shown in Fig. 3.2. The untouched impurity i is

²They are $|0\rangle$, $|\uparrow\rangle$, $|\downarrow\rangle$, and $|\uparrow\downarrow\rangle$.

³Otherwise, the Coulomb interaction (Eq. (2.7)) is distributed onto many new sites and is not local anymore.

3.1. Natural impurity orbitals and restricted active space

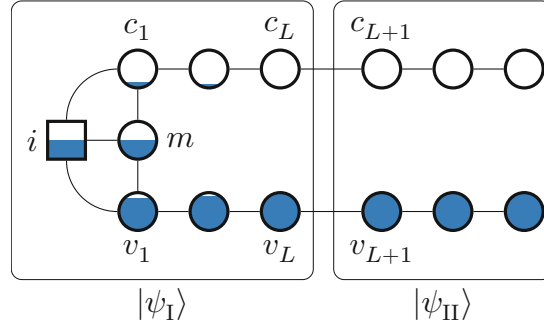


Figure 3.2.: Anderson impurity model in the natural orbital basis and subsequent separation of the wave function into two components $|\psi_I\rangle$ and $|\psi_{II}\rangle$ denoted by two boxes.

connected to a mirror site (labeled m) and two chains. Following the convention of [20, 21], we call sites in the almost fully filled chain valence bath sites (labeled v), and sites in the almost empty chain as conduction bath sites (labeled c). Hopping between sites is again shown by lines.

This transformation does not change the dimensionality of the Hilbert space. To alleviate the scaling problem we employ the restricted active space (RAS) method, which decomposes the wave function into two components

$$|\psi\rangle = |\psi_I\rangle \otimes |\psi_{II}\rangle \quad (3.6)$$

sketched in Fig. 3.2. For $|\psi_I\rangle$ we take all possible states into account. This is feasible because we fix the parameter L (the number of conduction and valence bath sites to be treated exactly) to be very small compared to the number of bath sites n : $L \ll n$.

In $|\psi_{II}\rangle$ which contains the remaining chain sites we neglect almost all possible states. In the simplest approximation (labeled $p = 0$) we enforce that all valence sites in $|\psi_{II}\rangle$ are fully filled (denoted by $|\mathbb{1}_v\rangle$) while conduction sites are completely empty (denoted by $|\mathbb{0}_c\rangle$). The wave function can thus be written as

$$|\psi_{II}\rangle = |\mathbb{1}_v\rangle \otimes |\mathbb{0}_c\rangle. \quad (3.7)$$

For $p = 1$ we (additionally to $p = 0$) allow one electron or one hole excitation. This creates additional possible states

$$|\mathbb{1}_v\rangle \otimes c_{k\sigma}^\dagger |\mathbb{0}_c\rangle, \quad (3.8a)$$

$$v_{k\sigma} |\mathbb{1}_v\rangle \otimes |\mathbb{0}_c\rangle. \quad (3.8b)$$

This can be further extended to $p = 2$ which (including all previous excitations) contains electron-electron, electron-hole, and hole-hole excitations

$$|\mathbb{1}_v\rangle \otimes c_{k\sigma}^\dagger c_{k'\sigma'}^\dagger |\mathbb{0}_c\rangle, \quad (3.9a)$$

$$v_{k\sigma} |\mathbb{1}_v\rangle \otimes c_{k'\sigma'}^\dagger |\mathbb{0}_c\rangle, \quad (3.9b)$$

$$v_{k\sigma} v_{k'\sigma'} |\mathbb{1}_v\rangle \otimes |\mathbb{0}_c\rangle. \quad (3.9c)$$

3. Numerical methods

Theoretically, one can continue this approach to higher and higher excitations with the limit of all excitations recovering the full Hilbert space (including the exponential growth of the available configurations). In this work we only implemented excitations up to $p = 2$, as higher p are not numerically feasible for hundreds of bath sites.

3.2. Lanczos algorithm

Even with RAS, the Hilbert space is still too large to decompose the Hamiltonian which is represented as an $r \times r$ matrix. Therefore, we use the Lanczos algorithm [38] as it has some nice properties for our given problem. First, it converges fastest to extremal eigenvalues which works very well for the ground state⁴. Secondly, it requires a hermitian matrix which our Hamiltonian is. Lastly it works very well if our matrix is sparse which is the case for our geometry⁵. The method is based on a Krylov basis

$$\mathcal{K}^M(H, \mathbf{q}) = \text{span}\{\mathbf{q}, H\mathbf{q}, H^2\mathbf{q}, \dots, H^{M-1}\mathbf{q}\} \quad (3.10)$$

for a given vector \mathbf{q} . Typically, the value M required for a good approximation is very small compared to the matrix size $M \ll r$. Instead of a simple power iteration, the Lanczos algorithm is described by the following recurrence relation

$$b_j \mathbf{q}_{j+1} = H\mathbf{q}_j - a_j \mathbf{q}_j - b_{j-1} \mathbf{q}_{j-1} \quad (3.11)$$

with a normalized starting vector \mathbf{q}_1 and $\mathbf{q}_0 = \mathbf{0}$. The coefficients are chosen such that each Lanczos vector is orthonormal to each other $\mathbf{q}_i^\dagger \mathbf{q}_j = \delta_{ij}$, i.e.,

$$a_j = \mathbf{q}_j^\dagger H \mathbf{q}_j, \quad b_j = \mathbf{q}_{j+1}^\dagger H \mathbf{q}_j. \quad (3.12)$$

For numerical stability [39, 40] we instead calculate the coefficients as

$$a_j = \mathbf{q}_j^\dagger (H\mathbf{q}_j - \beta_{j-1} \mathbf{q}_{j-1}), \quad b_j = \|H\mathbf{q}_j - \alpha \mathbf{q}_j - \beta_{j-1} \mathbf{q}_{j-1}\|. \quad (3.13)$$

From this relation we can create the tridiagonal matrix

$$T = \begin{pmatrix} a_1 & b_1 & & & \\ b_1 & a_2 & b_2 & & \\ & b_2 & a_3 & \ddots & \\ & & \ddots & \ddots & b_{M-1} \\ & & & b_{M-1} & a_M \end{pmatrix}, \quad (3.14)$$

and a matrix collecting all Lanczos vectors

$$Q = (\mathbf{q}_1, \mathbf{q}_2, \dots, \mathbf{q}_M). \quad (3.15)$$

Rewriting Eq. (3.11) in matrix form and rearranging results in $T = Q^\dagger H Q$, which means that T is the orthogonal projection of H onto the subspace $\mathcal{K}^M(H, \mathbf{q}_1)$ [41].

⁴Due to the variational principle it is the state with the lowest possible energy.

⁵As most bath sites are inside two long chains, almost all hopping elements are zero.

3.2.1. Block variant

Instead of calculating only one vector \mathbf{q}_j in each step, one can calculate s vectors simultaneously. We define

$$Q_1 = (\mathbf{q}_1^{(1)}, \mathbf{q}_1^{(2)}, \dots, \mathbf{q}_1^{(s)}) \quad (3.16)$$

to be an $r \times s$ orthonormal block of starting vectors $Q_1^\dagger Q_1 = \mathbb{1}_{s \times s}$ and $Q_0 = 0_{r \times s}$. Then the recurrence relation (Eq. (3.11)) can be rewritten as

$$Q_{j+1} B_j = H Q_j - Q_j A_j - Q_{j-1} B_{j-1}^\dagger, \quad (3.17)$$

with A_j, B_j matrices of size $s \times s$ set such that each block is orthonormal to each other $Q_i^\dagger Q_j = \mathbb{1}_{s \times s} \delta_{ij}$. The block tridiagonal matrix of size $Ms \times Ms$ is written as

$$T = \begin{pmatrix} A_1 & B_1^\dagger & & & & \\ B_1 & A_2 & B_2^\dagger & & & \\ & B_2 & A_3 & \ddots & & \\ & & \ddots & \ddots & B_{M-1}^\dagger & \\ & & & B_{M-1} & A_M & \end{pmatrix}. \quad (3.18)$$

For the calculation for B_j one needs to orthonormalize

$$\tilde{Q}_{j+1} = H Q_j - Q_j A_j - Q_{j-1} B_{j-1}^\dagger, \quad (3.19)$$

which is not unique. For instance, a QR decomposition $Q_{j+1} B_j = \tilde{Q}_{j+1}$ results in an upper triangular matrix B_j which gives T a compactly banded structure [41, 42]. In our work however, we use symmetric Löwdin orthonormalization [36, 43] which is based on the singular value decomposition $\tilde{Q}_{j+1} = U \Sigma V^\dagger$. We define the overlap matrix as

$$S := \tilde{Q}_{j+1}^\dagger \tilde{Q}_{j+1} = V \Sigma^2 V^\dagger \quad (3.20)$$

and its roots as

$$S^{1/2} = V \Sigma V^\dagger, \quad S^{-1/2} = V \Sigma^{-1} V^\dagger. \quad (3.21)$$

The resulting vectors are then

$$Q_{j+1} = \tilde{Q}_{j+1} S^{-1/2}, \quad (3.22)$$

$$B_j = S^{1/2}. \quad (3.23)$$

We use this method as it guarantees hermiticity in the off-diagonal blocks $B_j^\dagger = B_j$ albeit losing the compactly banded structure for T . If \tilde{Q}_j is rank-deficient, this method can still be applied [36] by only inverting the block of non-vanishing singular values

$$\Sigma = \begin{pmatrix} \Sigma_i \neq 0 & 0 \\ 0 & 0 \end{pmatrix} \quad \Sigma^{-1} = \begin{pmatrix} \Sigma_i^{-1} & 0 \\ 0 & 0 \end{pmatrix}, \quad (3.24)$$

still guaranteeing orthogonality against previous states $Q_i^\dagger Q_j = 0_{s \times s}$ for $i \in \{1, \dots, j-1\}$ [42].

3.3. Ground state

Before we can calculate any expectation value or correlators, we first need to obtain the ground state of our impurity problem.

As an initial guess we take the state with all valence bath sites v_k filled in combination with a singlet state⁶ in the impurity d and mirror site m

$$|\psi_s\rangle = \frac{1}{\sqrt{2}} \left(d_{\uparrow}^{\dagger} m_{\downarrow}^{\dagger} - d_{\downarrow}^{\dagger} m_{\uparrow}^{\dagger} \right) \prod_{k\sigma} v_{k\sigma}^{\dagger} |0\rangle. \quad (3.25)$$

Given this state, we can calculate an approximate ground state energy

$$E_s = \langle \psi_s | H | \psi_s \rangle \quad (3.26)$$

and shift our Hamiltonian according to Eq. (2.15). This allows us to calculate a variance

$$\text{Var}_s = \langle \psi_s | H^2 | \psi_s \rangle, \quad (3.27)$$

which is not going to be very accurate. To get a better approximation, we employ the aforementioned Lanczos method (Sec. 3.2) with restarting as described in [20]: Given an approximate ground state $|\psi^{(i)}\rangle$, we calculate a new Krylov basis $\mathcal{K}^5(H, |\psi^{(i)}\rangle)$ which is diagonalized. From this, we calculate a new state $|\psi^{(i+1)}\rangle$ with a new ground state energy $E^{(i+1)}$ and variance $\text{Var}^{(i+1)}$. This loop is repeated until the variance falls below a given tolerance as it must vanish for a true eigenstate of H .

One should note that even if the variance is exactly zero for a state $|\tilde{\psi}_0\rangle$ in RAS, this state is not a true eigenstate of the unrestricted Hamiltonian. Applying H on $|\tilde{\psi}_0\rangle$ without any restriction will generate new states [20] that were not accounted for.

3.4. Correlator representation

In the following we will use the notation $\omega + i0^+ \triangleq (\omega + i0^+) \mathbb{1}$ for a diagonal matrix and $\frac{1}{K}$ for the matrix inverse K^{-1} . Using the Lanczos algorithm, we can obtain diagonal correlators by using $A^{\dagger} |\psi_0\rangle$ or $A |\psi_0\rangle$ as our input vector $\tilde{\mathbf{q}}_1$. By storing its norm⁷ $b_0 = \|\tilde{\mathbf{q}}_1\|$ and subsequent normalization $\mathbf{q}_1 = \tilde{\mathbf{q}}_1/b_0$ we obtain the correlator as the first component of the inverse of our tridiagonal matrix T [20],

$$C_{\omega}^{\pm} = b_0 \left[\frac{1}{\omega + i0^+ \mp T} \right]_{11} b_0. \quad (3.28)$$

This can be expanded to calculate block correlators where we apply multiple operators onto $|\psi_0\rangle$ simultaneously. Here, the subscript K_{11} is meant as the first $s \times s$ block of the matrix K

$$C_{\omega}^{\pm} = B_0 \left[\frac{1}{\omega + i0^+ \mp T} \right]_{11} B_0. \quad (3.29)$$

⁶We do not want any magnetic moment in SU(2) symmetry.

⁷ b_0 therefore contains information about the zeroth moment $C^{(0)}$.

3.4. Correlator representation

Thus, the scalar case returns one correlator while the block version returns s^2 correlators simultaneously.

Using the Schur complement [44], we can directly take our coefficients given in Eqs. (3.14) and (3.18) and represent correlators as a continued fraction

$$C_\omega = \frac{b_0^2}{\omega + i0^+ - a_1 - \frac{b_1^2}{\omega + i0^+ - a_2 - \dots}}, \quad (3.30a)$$

$$C_\omega = B_0 \frac{1}{\omega + i0^+ - A_1 - B_1 \frac{1}{\omega + i0^+ - A_2 - \dots} B_1} B_0. \quad (3.30b)$$

In contrast to QUANTY [45] we always keep our matrices B_i hermitian, even if they are rank-deficient.

Diagonalizing the matrix T allows us to represent (block) correlators as a sum of poles:

$$C_\omega = \sum_{i=1}^M \frac{w_i}{\omega + i0^+ - \epsilon_i}, \quad (3.31a)$$

$$C_\omega = \sum_{i=1}^{Ms} \frac{W_i}{\omega + i0^+ - \epsilon_i}, \quad (3.31b)$$

where M is the Krylov size and s the size of each block. As we calculate diagonal elements, all weights w_i (scalar) are positive or W_i (matrix) positive semidefinite. To simplify the sum, we merge degenerate locations and list them in increasing order such that $\epsilon_i < \epsilon_{i+1}$.

Only diagonalizing from the second entry of T onwards gives us the *Anderson representation*

$$C_\omega = \frac{b_0^2}{\omega + i0^+ - a_1 - \sum_j \frac{w_j}{\omega + i0^+ - \epsilon_j}}, \quad (3.32a)$$

$$C_\omega = B_0 \frac{1}{\omega + i0^+ - A_1 - \sum_j \frac{W_j}{\omega + i0^+ - \epsilon_j}} B_0, \quad (3.32b)$$

which is helpful to calculate inverses of (block) correlators.

A detailed explanation on how to transform between these representations is given in [20].

We calculate the correlators listed in Eq. (2.33) as

$$C_\omega^+ = \left\langle \psi_0 \left| \begin{pmatrix} \tilde{q}_\sigma \\ d_\sigma \end{pmatrix} \frac{1}{\omega + i0^+ - H} \begin{pmatrix} \tilde{q}_\sigma^\dagger & d_\sigma^\dagger \end{pmatrix} \right| \psi_0 \right\rangle = \begin{pmatrix} I_\omega^+ & F_\omega^{L+} \\ F_\omega^{R+} & G_\omega^+ \end{pmatrix}, \quad (3.33a)$$

$$C_\omega^- = \left\langle \psi_0 \left| \begin{pmatrix} \tilde{q}_\sigma^\dagger \\ d_\sigma^\dagger \end{pmatrix} \frac{1}{\omega + i0^+ + H} \begin{pmatrix} \tilde{q}_\sigma & d_\sigma \end{pmatrix} \right| \psi_0 \right\rangle = \begin{pmatrix} I_\omega^- & F_\omega^{R-} \\ F_\omega^{L-} & G_\omega^- \end{pmatrix} \quad (3.33b)$$

3. Numerical methods

and add them together

$$C_\omega = C_\omega^+ + (C_\omega^-)^\top = \begin{pmatrix} I_\omega & F_\omega^L \\ F_\omega^R & G_\omega \end{pmatrix}. \quad (3.34)$$

Thus, our block size is $s = 2$. In [25] it was noted that $F_\omega^R = (F_\omega^L)^\dagger$ might be violated numerically. We do not have this problem as all matrices A_i and B_i are hermitian, and thus C_ω is also hermitian⁸.

3.4.1. Broadening

In this work we calculate the whole DMFT self-consistency on the real axis with discrete poles. However, this gives issues when we want to plot the spectral part of our correlators. Applying Eq. (2.19) to our representation from Eq. (3.31) gives discrete delta-peaks

$$A_\omega = \sum_i w_i \delta(\omega - \epsilon_i). \quad (3.35)$$

Thus, to get smooth spectra we broaden the peaks and obtain the real part through Eq. (2.20a). We will denote the broadened correlator as C_z to contrast it against C_ω which has no broadening. In this work we will use the following three methods

- (i) Lorentzian broadening characterized by δ :

$$\delta(\omega - \omega_0) \rightarrow \frac{1}{\pi} \frac{\delta}{(\omega - \omega_0)^2 + \delta^2}, \quad (3.36)$$

- (ii) Gaussian broadening characterized by σ :

$$\delta(\omega - \omega_0) \rightarrow \frac{1}{\sqrt{2\pi\sigma^2}} \exp\left(-\frac{(\omega - \omega_0)^2}{2\sigma^2}\right), \quad (3.37)$$

- (iii) logarithmic Gaussian characterized by b [16]:

$$\delta(\omega - \omega_0) \rightarrow \Theta(\omega\omega_0) \frac{e^{-b^2/4}}{b\omega_0\sqrt{\pi}} \exp\left(-\frac{(\ln \omega - \ln \omega_0)^2}{b^2}\right). \quad (3.38)$$

A comparison of these broadenings for a correlator $C_\omega = \frac{1}{\omega+i0^+-0.25} + \frac{0.5}{\omega+i0^+-1}$ is given in Fig. 3.3. The Lorentzian and Gaussian spectra consist of symmetric peaks with the former decaying slower compared to the latter. The peaks generated by the logarithmic Gaussian are asymmetric and sharper if the pole is closer to $\omega = 0$. As all poles are located at $\omega > 0$, the spectrum of the log Gaussian vanishes for $\omega \leq 0$.

Given our spectrum as discrete peaks (Eq. (3.35)), we can easily calculate the moments of a correlator (defined in Eq. (2.23))

$$C^{(n)} = \int_{-\infty}^{\infty} d\omega \omega^n \sum_i w_i \delta(\omega - \epsilon_i) = \sum_i w_i \epsilon_i^n. \quad (3.39)$$

⁸Due to floating-point arithmetic it can happen that hermiticity is violated for the least significant digit. This is avoided by setting matrices to $K \rightarrow 1/2(K + K^\dagger)$.

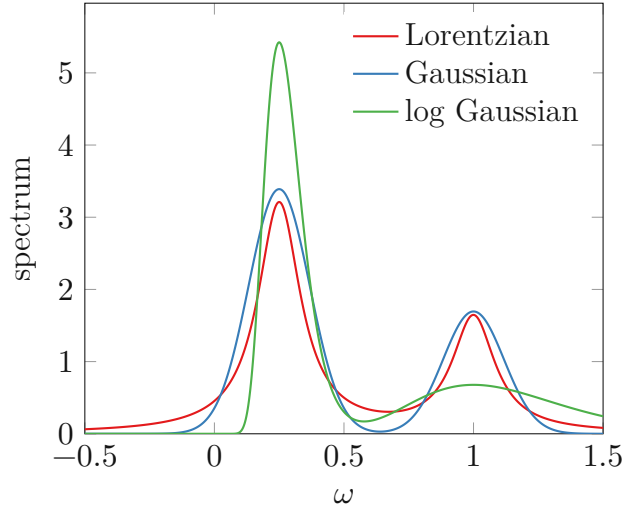


Figure 3.3.: Spectral part of a correlator $C_\omega = \frac{1}{\omega+i0^+-0.25} + \frac{0.5}{\omega+i0^+-1}$ using various broadening schemes.

3.5. Self-energy calculation

In [20], the Dyson equation (Eq. (2.27)) was used to represent the self-energy by the constant Hartree term Σ^H and a sum of poles

$$\Sigma_\omega = \Sigma^H + \sum_i \frac{w_i}{\omega + i0^+ - \epsilon_i}. \quad (3.40)$$

As the self-energy is also analytical in the upper complex plane, all weights must be positive. On a system with finite bath sites and floating-point arithmetic however, this is numerically violated, and poles with negative weight must be merged into neighbors such that only positive weight remains.

To avoid this issue, we use the symmetric improved estimator [25]. Kugler calculated each correlator from Eq. (2.33) broadened on a grid and then the self-energy Σ_z . In this work we instead calculate the self-energy on the real axis using the Schur complement [35, 44]

$$\Sigma_\omega = \Sigma^H + ([(C_\omega)^{-1}]_{11})^{-1}. \quad (3.41)$$

To invert our block correlation function, we first bring it to the Anderson representation (Eq. (3.32)):

$$C_\omega = B \frac{1}{\omega + i0^+ - A - D_\omega} B, \quad (3.42)$$

with 2×2 matrices A , B and D_ω representing a 2×2 block sum of poles (Eq. (3.31)). The scaling matrix B contains the square root of the zeroth moments, and is

$$B = \begin{pmatrix} U/2 & 0 \\ 0 & 1 \end{pmatrix} \quad (3.43)$$

3. Numerical methods

at half-filling. Diagonality comes from the shift in Eq. (2.32). The Schur complement is then

$$((C_\omega)^{-1})_{11}^{-1} = B_{11} \frac{1}{\omega + i0^+ - A_{11} - (D_\omega)_{11}} B_{11}. \quad (3.44)$$

Diagonalizing this expression gives us the self-energy in the same form as Eq. (3.40). Contrasting against Eq. (2.27), all pole weights are positive by construction and no merging of negative weight into neighbors is necessary.

Given our pole representation in Eq. (3.40), we can calculate the quasiparticle weight in Fermi-liquid theory⁹ [2] analytically

$$\begin{aligned} Z &= \left(1 - \left. \frac{\partial \text{Re } \Sigma_\omega}{\partial \omega} \right|_{\omega=0} \right)^{-1}, \\ &= \left(1 + \sum_i \frac{w_i}{\epsilon_i^2} \right)^{-1}, \\ &= (1 + \Sigma^{(-2)})^{-1} \end{aligned} \quad (3.45)$$

with the negative second moment $\Sigma^{(-2)}$. We see that the expression inside the brackets diverges if there is a pole at $\epsilon_i = 0$, which is the case for an insulator [7]. In a metal, the low energy expansion of the self-energy is [2]

$$-\text{Im } \Sigma = a\omega^2 + bT^2, \quad (3.46)$$

which vanishes at the Fermi-energy for zero temperature. Thus, in the metallic region we have no pole located at zero¹⁰.

In [46, 47] it was suggested to calculate the quasiparticle weight using Eq. (A.18) applied on the impurity Green's function

$$Z = \frac{2}{D^2} \left(\left. \frac{\partial G_\omega}{\partial \omega} \right|_{\omega=0} \right)^{-1}. \quad (3.47)$$

This is not possible in our method, as the metallic Green's function has a pole located at zero which gives a divergence.

⁹Instead of interacting particles, non-interacting quasiparticles are used to describe a system. These get, e.g., a renormalized mass $m^* = m/Z$ where m is the electron mass. For a non-interacting system $Z = 1$ by construction.

¹⁰We will discuss this statement for our discrete model in Sec. 4.6.

4. Results

In this chapter we show results for our DMFT solver on the Bethe lattice in infinite dimensions and at half-filling. We study the Mott metal-to-insulator transition by continuously varying the Coulomb interaction U . Calculations were done using Julia [48] version 1.11 and 1.12. The codebase is contained in two packages: `Fermions.jl` [37] implements Hamiltonians, wave functions and their interplay. The second package `RAS_DMFT.jl`¹, which was developed during this work, contains the DMFT self-consistency loop together with the representation of correlators and self-energies. A tutorial of the latter is available in [App. B](#).

For all following calculations we set the half-bandwidth $D = 1$ as our unit of energy. For the discretization of our hybridization function Δ_ω we use an odd number of bath sites N with $(N - 1)/2$ poles on the positive and negative axis respectively and one pole at exactly zero. The locations of these poles $\{\epsilon_i\}$ are fixed at the beginning and kept between each DMFT cycle. This is in contrast to [20, 21] where the locations could shift in each iteration. If, in the DMFT update (Eq. (2.39)), we get a pole ϵ which is not on the given grid, we shift its weight such that the zeroth and first moment are locally conserved. This scheme is explained in [App. A.3](#). The poles of correlators and self-energies are not put onto this predefined grid. Before the first DMFT step, the continuous hybridization function is discretized on the aforementioned locations with weights

$$V_i^2 = -\frac{1}{\pi} \int_{I_i} d\omega \operatorname{Im} \Delta_{0,\omega}. \quad (4.1)$$

The interval endpoints are chosen to be halfway between neighboring bath energies

$$I_i = \left[\frac{\epsilon_{i-1} + \epsilon_i}{2}, \frac{\epsilon_i + \epsilon_{i+1}}{2} \right]. \quad (4.2)$$

The lower bound for the first point is set to $-\infty$ while the upper bound for the last point is $+\infty$. This asserts that the sum of all discrete weights equals the zeroth moment of the continuous function². The following DMFT self-consistency calculations were done on $N = 301$ bath sites and a Krylov space $M = 200$ to be comparable to [21]. (Each block Lanczos step produces two poles which is equivalent to $M = 400$ for scalar Lanczos.)

¹https://github.com/frankebel/RAS_DMFT.jl

²The zeroth moment is conserved exactly while higher moments are not. The higher the moment, the more it differs between the discrete and continuous one. Odd moments stay zero as the discrete function is still symmetric.

4. Results

4.1. Ground state convergence

Before we can calculate any correlators or expectation values, we first need to find the ground state of our system. The hybridization function, is discretized on $N = 101$ equidistant bath sites in the interval $[-D, D]$. Given the parameters $\{\epsilon_i, V_i\}$, we can create H_{bath} and $H_{\text{imp-bath}}$ of Eqs. (2.8) and (2.9). For the impurity H_{imp} we then add a Coulomb interaction of $U = 2D$ which fixes our on-site energy to $\epsilon = -D$, $\mu = 0$ for half-filling, only nearest-neighbor hopping. We can then iteratively find our ground state using the algorithm described in Sec. 3.3. The variance after each restart is shown in Fig. 4.1. We see that it decreases exponentially with the number

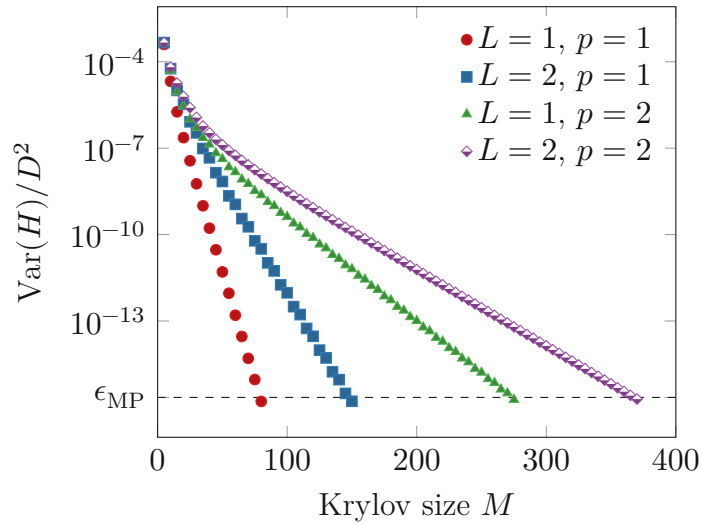


Figure 4.1.: Krylov space convergence: Variance of the Hamiltonian on a state $|\psi\rangle$ calculated by the Lanczos algorithm from Sec. 3.3. For the ground state the variance must vanish. The dashed line indicates double precision machine epsilon 2^{-52} .

of restarts and reaches below double precision $\epsilon_{\text{MP}} = 2^{-52}$. Although not shown, this is also the case for other values of U . In general, the bigger the explored Hilbert space (increasing the exact system size L and allowed excitations p in the remaining chains), the more steps are necessary to reach a desired variance. For the parameters $L = 1, p = 1$, machine precision is reached after 16 iterations which equals a Krylov size³ of $M = 80$, while for higher parameters L, p more steps are necessary for a desired variance. To fully propagate an electron (hole) excitation through the conduction (valence) band, one should at least explore a space of $M = N/2$ where $N/2$ is the length of a chain. For our choice of $N = 101$ this corresponds to $M = 50$ which is fulfilled for all cases. In Tab. 4.1 we list the ground state energy E_0 obtained in the calculation of Fig. 4.1. We see that the values are very close to each other with an absolute difference of less than one per mille of the bandwidth. As expected, the energy is lower if the explored Hilbert space is larger.

³Each restart explores a further space of \mathcal{K}^5 .

Table 4.1.: Ground state energy E_0 of the half-filled Anderson impurity model at $U = 2D$ on 101 bath sites for parameters L, p . The energy difference is less than one per mille of the half-bandwidth D of the conduction electrons.

L	p	E_0/D
1	1	-52.29489
1	2	-52.29516
2	1	-52.29518
2	2	-52.29522

4.2. Performance analysis

To obtain our correlators listed in Eq. (2.33), we have to calculate a block tridiagonal matrix T using the block Lanczos algorithm explained in Sec. 3.2.1. As this is the most time-consuming part within the DMFT step, we benchmarked its time and memory requirements in Fig. 4.2. For each data point we ran the same calculation ten times and show the minimum as our estimator [49]. The operations were done on an AMD EPYC™ 9654 processor with 96 cores and 1 TB of memory, but can also be run on consumer hardware. Although the code is multithreaded, the benchmarks were run on a single thread for easier reproducibility. Given the ground state, we create the excited states $\tilde{q}_\sigma^\dagger|\psi_0\rangle$ and $d_\sigma^\dagger|\psi_0\rangle$ as our block Lanczos input allowing us to calculate the partial correlator C_ω^+ on the positive real axis. In Fig. 4.2(a), we fixed the number of bath sites to $N = 161$. We see that the runtime is linear with the number of Krylov steps M . This is expected as our wave function representation stores determinants in the restricted part $|\psi_{\text{II}}\rangle$ in a dense format. As all possible states are already present in the first step, each subsequent Lanczos iteration takes the same amount of time resulting in a linear scaling. Fig. 4.2(c) shows the used memory during calculations. We see an almost constant behavior. This is because the Lanczos algorithm only needs the last two states for orthogonalization. Thus, we can overwrite the oldest state in-place in each iteration. However, there are still some allocations of the order 10 MB coming from matrix diagonalization and matrix multiplication. These allocations are negligible on current hardware which has multiple GB of memory.

In Fig. 4.2(b) we analyze the time required for a fixed number of Krylov steps $M = 160$ by varying the number of bath sites N . For the restricted excitation, the number of possible states is

$$\binom{2(N-1-2L)}{p}, \quad (4.3)$$

where the factor 2 accounts for two spin states at each site, and the reduction of sites results from only looking at part of the chains. For $N \gg L$ and $N \gg p$ (we are using $L, p \in \{1, 2\}$), the scaling of the binomial coefficient can be written as N^p .

4. Results

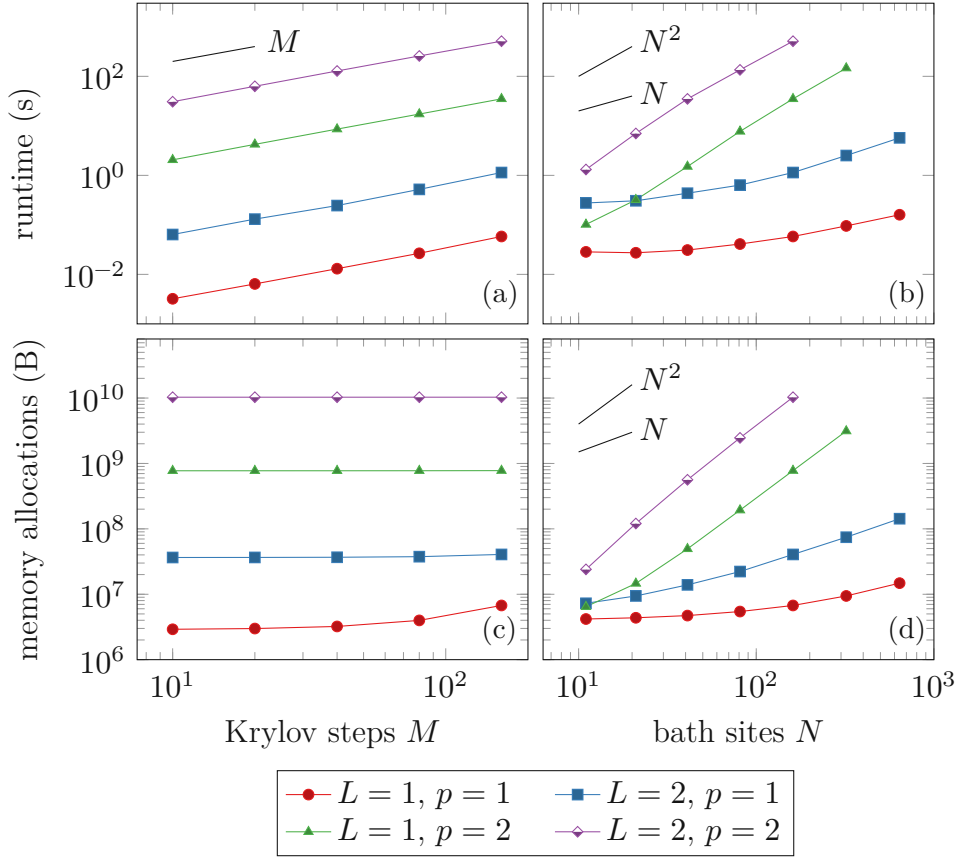


Figure 4.2.: Runtime and total memory allocations to obtain the block correlator on the positive real axis C_ω^+ using the block Lanczos algorithm described in Sec. 3.2.1. Given the ground state, the benchmarked task is to create the vectors $\tilde{q}_\sigma^\dagger|\psi_0\rangle$ and $\tilde{d}_\sigma^\dagger|\psi_0\rangle$ as our input. In (a), (c) we fix the number of bath sites to $N = 161$. In (b), (d) we fix the number of Krylov steps to $M = 160$.

Thus, for $p = 1$ we see a linear scaling with increased bath sites while for $p = 2$ it is quadratic. We also see that raising the parameter L (the number of chain sites treated exactly) by one increases the complexity by a factor of more than ten. A calculation of all possible states⁴ reveals a ratio of around 14 which is relatively close to the measured one. Fig. 4.2(d) shows the required memory for those calculations which scales as N and N^2 , too.

In summary, we can say that our computational complexity scales approximately as $O(14^L M N^p)$ while memory complexity scales as $O(14^L N^p)$.

⁴The exact number depends on the values of N and p too. For the relevant regime the complexity by increasing L by one unit varies between 12 and 14. To emphasize the worst scaling, we take the value of 14 in the main text. Full details are available in App. A.4.

4.3. Correlators

For the following calculations we first define $N = 301$ equidistant poles $\{\epsilon_i\}$ in the interval $[-4D, 4D]$ and discretize the non-interacting hybridization function $\Delta_{0,\omega}$ on them. Poles outside $[-D, D]$ have zero weight. Thus, our non-interacting hybridization has 75 non-vanishing poles. We then repeat our DMFT loop which calculates a new hybridization function Δ_ω in each step until self-consistency is reached. As the self-energy pushes spectral weight to higher frequencies, poles which initially had zero weight obtain a finite value. The explored Hilbert space is restricted to $L = 2, p = 2$. In Fig. 4.3 we list the real and imaginary parts of our block correlator C_ω for a metallic solution $U/D = 2$. Each discrete pole was broadened

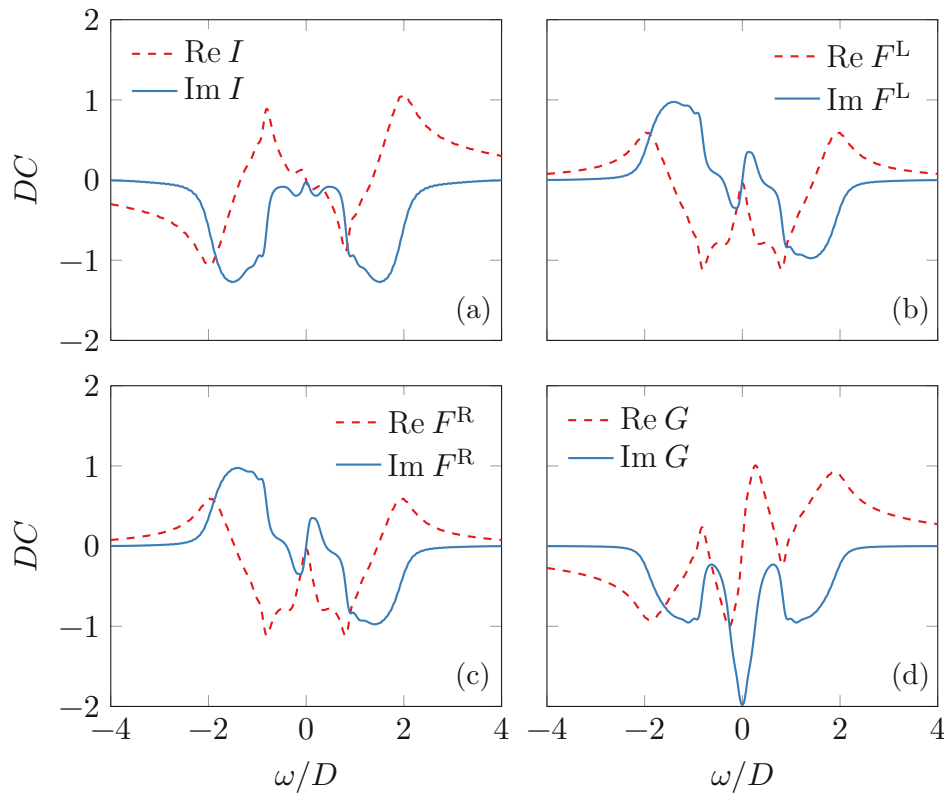


Figure 4.3.: Components of the 2×2 block correlator C_ω for a Coulomb interaction of $U = 2D$ (metallic solution). Peaks are broadened with a Gaussian kernel $\sigma/D = 0.04$. At half-filling, the spectral part (imaginary part) of (a) and (d) are symmetric. Due to the shift of Eq. (2.32), the spectra of (b) and (c) are antisymmetric.

with a Gaussian kernel $\sigma/D = 0.04$. We see that the spectra (imaginary part) of the diagonal entries Figs. 4.3(a) and 4.3(d) are symmetric due to particle-hole symmetry. The imaginary part is negative (the spectrum positive semidefinite) as the weight w_i of each pole is positive. The spectra of the offdiagonal entries Figs. 4.3(b) and 4.3(c) are antisymmetric due to the shift in Eq. (2.32). As we use real-valued amplitudes, the

4. Results

condition $F_\omega^R = (F_\omega^L)^\dagger$ simplifies to $F_\omega^R = F_\omega^L$. Using these symmetries, it is possible to only calculate C_ω^+ and mirror the entries for C_ω^- with an appropriate sign flip. This was deliberately not done in this work to show that symmetry is conserved even numerically.

In Fig. 4.4 we show the same quantities for an insulating solution $U/D = 4.0$. The symmetry arguments are the same. In contrast to the metallic solution however, none of the spectra show any weight at the Fermi-energy.

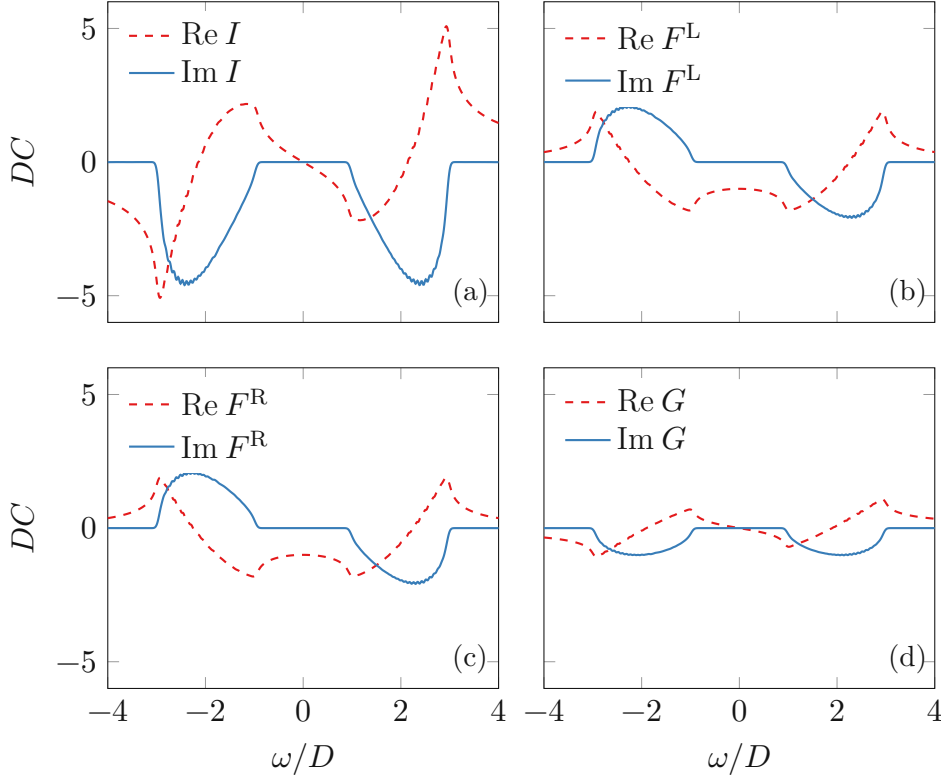


Figure 4.4.: Components of the 2×2 block correlator C_ω for a Coulomb interaction of $U = 4D$ (insulating solution). Peaks are broadened with a Gaussian kernel $\sigma = 0.04D$. At half-filling, the spectral part (imaginary part) of (a) and (d) are symmetric. Due to the shift of Eq. (2.32), the spectra of (b) and (c) are antisymmetric.

4.4. Spectral function

We again emphasize that the self-consistency calculation uses no-broadening, which is only introduced as a post-processing step to plot smooth spectra instead of discrete peaks. Numerically we never get a pole at exactly zero which is why strictly speaking, all of our solutions are insulating. For a $p = 1$ projection (not shown) we observe spurious oscillations on the Hubbard bands, consistent with [21]. These are suppressed if we increase the Hilbert space to $p = 2$, as shown in Fig. 4.5 for $L = 2$. For each

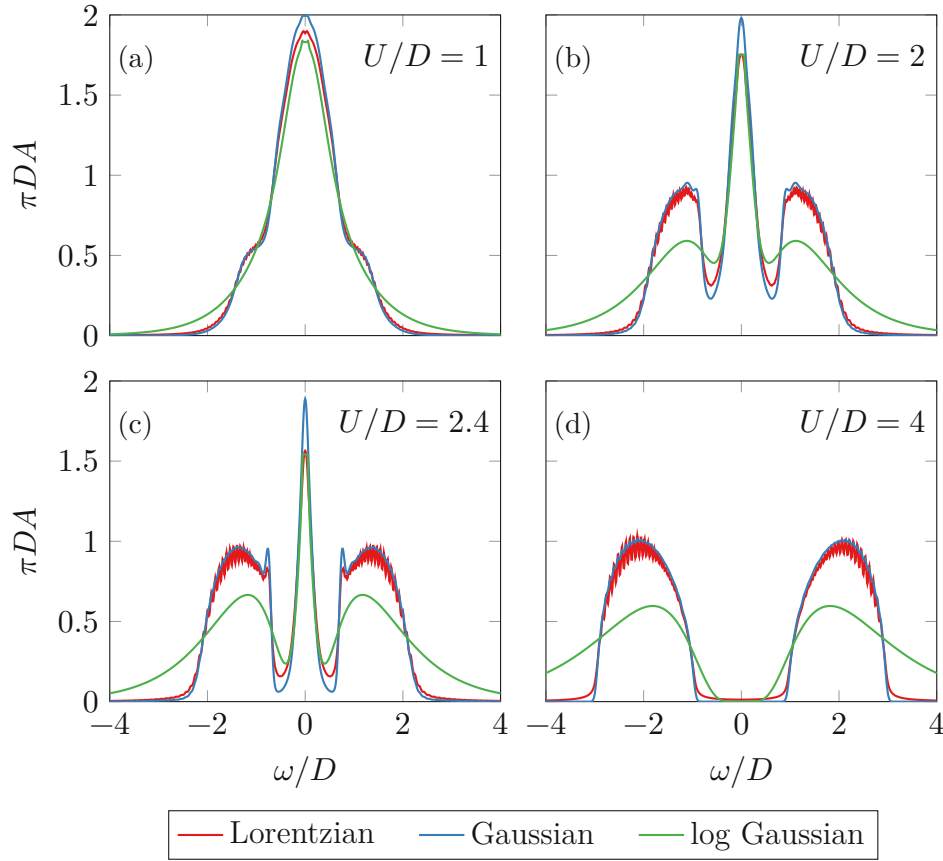


Figure 4.5.: DMFT impurity spectral function A_ω for the half-filled Bethe lattice. (a), (b), (c) show the evolution of the Hubbard bands and Kondo peak with increasing interaction strength U . (d) shows an insulating solution where the bands are fully disconnected. For each value of U , we plot the same data using a Lorentzian ($\delta/D = 0.04$), Gaussian ($\sigma/D = 0.04$), and logarithmic Gaussian ($b/D = 0.6$) broadening.

fixed value of the Coulomb interaction U , we plot the same data using a Lorentzian ($\delta/D = 0.04$), Gaussian ($\sigma/D = 0.04$), and logarithmic Gaussian ($b/D = 0.6$) broadening. As we do not get our poles on a logarithmic grid, the latter had to be truncated at a rather large value of $\omega/D = 5 \cdot 10^{-2}$ to generate smooth spectra⁵. At small interaction Fig. 4.5(a) we see the beginning of the Hubbard band formation. We see a small dip at the Fermi-energy, as there are no poles very close to it. This is in contrast to NRG [16] which is tailored to impurity problems by utilizing a logarithmic grid. If we increase the interaction Fig. 4.5(b), we can see fully formed Hubbard bands and the central Kondo peak. At $U/D = 2.4$ in Fig. 4.5(c), we see small peaks in the inner edge of the Hubbard band, consistent with previous results [20, 21, 46, 47, 50–55]. In Fig. 4.5(d) we show an insulating solution; The bands are fully separated and peaked at approximately $\pm U/2$. The shape is approximately the

⁵Therefore, in the interval $\omega/D \in [-5 \cdot 10^{-2}, 5 \cdot 10^{-2}]$ the spectrum is set to a constant value.

4. Results

non-interacting semicircular density. As the Lorentzian broadening decays slowly, there is still some weight left at the Fermi-energy.

As the imaginary part of the self-energy vanishes at the Fermi-energy for zero temperature [2], any *metallic* spectral function must have the same value as the non-interacting one. This forces the pinning of the Kondo peak to a height of $\pi DA(\omega = 0) = 2.0$. We see that this is well fulfilled for the top two panels using Gaussian broadening, while in Fig. 4.5(c) this is slowly lost. In general, for the chosen parameters the Gaussian broadening shows all features well while the logarithmic broadening smears out too much at higher energies. This may be mitigated by using more advanced broadening schemes [56].

The DMFT calculation was also tried using a logarithmic grid with pole locations fixed to have equal ratio $\epsilon_{i+1}/\epsilon_i = \Lambda = 1.075$ [16] and the outermost pole located at $\epsilon_N = 4D$. The Kondo peak and pinning condition were marginally improved while the Hubbard bands showed discretization artifacts under the same broadening parameters.

In Tab. 4.2 we compare the moments of our Green's function against the exact ones from Eq. (2.26). The zeroth moment matches up to numerical precision $O(\epsilon_{\text{MP}})$ while higher moments differ around $O(\sqrt{\epsilon_{\text{MP}}})$. This is in contrast to NRG [16, 25] which only conserves the lowest order while higher ones are less accurate. We also see no inherent bias in the data as we both over- and underestimate the exact values.

Table 4.2.: Difference $\Delta G^{(n)}$ of the n -th moment of the impurity Green's function G to the exact value.

U/D	$\Delta G^{(0)}$	$\Delta G^{(1)}$	$\Delta G^{(2)}$	$\Delta G^{(3)}$
1.0	$4.22 \cdot 10^{-15}$	$-2.52 \cdot 10^{-8}$	$-7.99 \cdot 10^{-8}$	$4.26 \cdot 10^{-7}$
2.0	$1.11 \cdot 10^{-15}$	$5.30 \cdot 10^{-8}$	$1.54 \cdot 10^{-8}$	$-4.32 \cdot 10^{-8}$
2.4	$-8.88 \cdot 10^{-16}$	$3.81 \cdot 10^{-7}$	$5.23 \cdot 10^{-9}$	$-5.89 \cdot 10^{-7}$
4.0	$-4.55 \cdot 10^{-15}$	$-4.30 \cdot 10^{-9}$	$-7.63 \cdot 10^{-10}$	$1.25 \cdot 10^{-8}$

4.5. Self-energy

Given our correlators, we calculate the self-energy using the symmetric improved estimator [25]. In Fig. 4.6, we show the negative imaginary part for varying values of the Coulomb interaction U . We use the same broadening parameters for a Lorentzian ($\delta/D = 0.04$), Gaussian ($\sigma/D = 0.04$), and logarithmic Gaussian ($b/D = 0.6$) broadening as the spectra in the previous section. For a metallic solution [Figs. 4.6(a) to 4.6(c)] we see a two-peak structure. At $\omega = 0$, the imaginary part must vanish which can be seen in the Gaussian and logarithmic Gaussian broadening. Due to the slow decay of the Lorentzian, it still has some residual spectral weight. With increasing interaction, the magnitude of the two peaks rise, and the locations of the maxima move closer together.

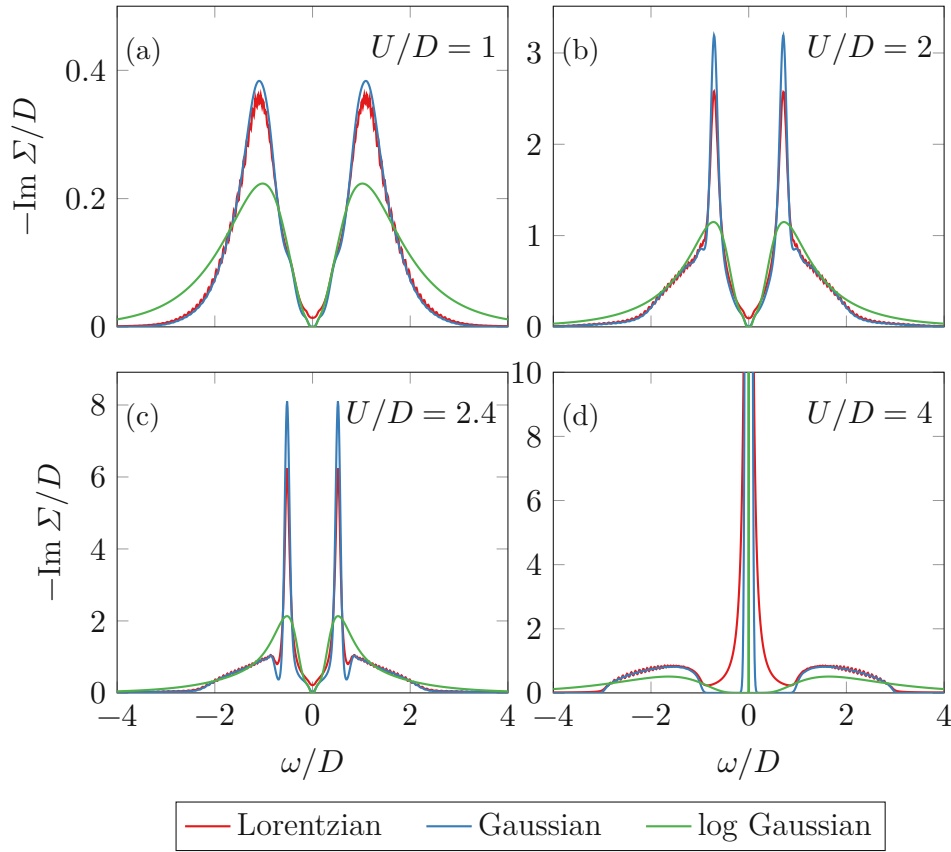


Figure 4.6.: DMFT impurity self-energies for the half-filled Bethe lattice. (a), (b), (c) show the two-peak structure with a vanishing self-energy at $\omega = 0$. (d) shows an insulating solution which diverges at $\omega = 0$. For each value of U , we plot the same data using a Lorentzian ($\delta/D = 0.04$), Gaussian ($\sigma/D = 0.04$), and logarithmic Gaussian ($b/D = 0.6$) broadening.

For an insulating solution (Fig. 4.6(d)), the two peaks merge to a diverging pole at $\omega = 0$. This pole should be infinitely thin, which is approximated well with the logarithmic broadening. For the Lorentzian and Gaussian broadening however, it gains a finite width. To better illustrate this, we plot the discrete locations and weights in Fig. 4.7. Here, we directly see that the spectral density vanishes within a gap $\omega \in [-\Delta_g/2, \Delta_g/2]$ with a singular pole located at $\omega = 0$ [7]. The central pole has the parameters

$$\frac{w_0}{\omega + i0^+ - \epsilon_0} = \frac{3.20}{\omega + i0^+ + 8.83 \cdot 10^{-8}}. \quad (4.4)$$

We see that the location is approximated very well by zero. For the weight, we can compare it against the relation [7]

$$w_0^{-1} = \int_{-\infty}^{\infty} d\omega \frac{A_\omega}{\omega^2} = G^{(-2)}, \quad (4.5)$$

4. Results

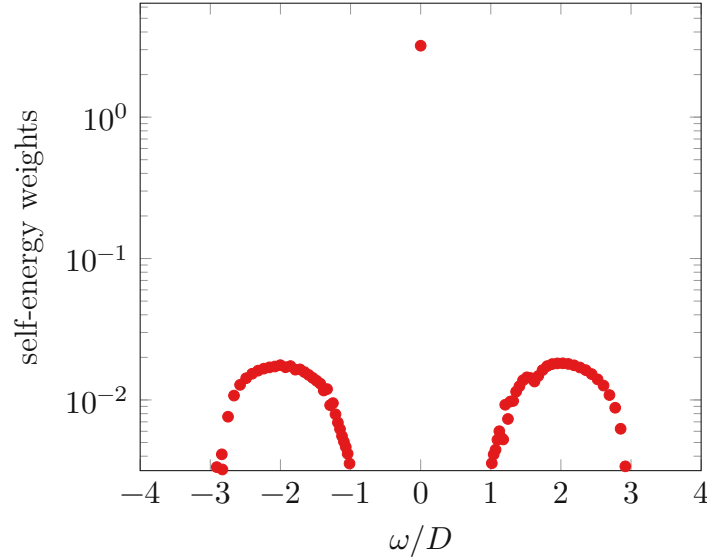


Figure 4.7.: Discrete poles of the insulating self-energy at $U/D = 4$. The spectral density vanishes within a gap $\omega \in [-\Delta_g/2, \Delta_g/2]$ with a singular pole located at $\omega = 0$ [7].

which matches up to seven digits.

Finally in Tab. 4.3, we compare the moments of the self-energy against the exact ones from Eq. (2.29). Similarly to the spectra, the zeroth moment is exact up to machine precision $O(\epsilon_{\text{MP}})$ while other moments differ around $O(\sqrt{\epsilon_{\text{MP}}})$. Also, there seems to be no bias in over- or underestimating of values.

Table 4.3.: Difference $\Delta\Sigma^{(n)}$ of the n -th moment of the self-energy Σ to the exact value. Σ^{H} is the Hartree term.

U/D	$\Delta\Sigma^{\text{H}}$	$\Delta\Sigma^{(0)}$	$\Delta\Sigma^{(1)}$
1.0	$-2.51 \cdot 10^{-8}$	$-3.33 \cdot 10^{-16}$	$2.46 \cdot 10^{-8}$
2.0	$5.31 \cdot 10^{-8}$	$-1.31 \cdot 10^{-14}$	$-1.80 \cdot 10^{-7}$
2.4	$1.31 \cdot 10^{-7}$	$4.66 \cdot 10^{-15}$	$-6.71 \cdot 10^{-7}$
4.0	$-2.03 \cdot 10^{-8}$	$-1.29 \cdot 10^{-14}$	$6.46 \cdot 10^{-8}$

4.6. Mott transition

As shown in the previous sections, depending on the interaction strength U we can get a metallic or insulating solution. Here, we want to quantify this transition. If one starts from a metallic solution, the transition to an insulator is of second order [7]. The ground state energy (which is lower for a metal) smoothly approaches that of an insulator and coincides at the critical value U_{c2} . In contrast, the transition of an insulator to metal is of first order [7] with a metastable solution which abruptly

jumps at a critical value U_{c1} . In the coexistence region $U_{c1} \leq U \leq U_{c2}$ it is possible to find both solutions.

One way of quantifying this region is to use the double occupation $\langle n_{\uparrow}n_{\downarrow} \rangle$, which is the ground state probability of finding both a spin-up and spin-down electron in the impurity. The results are shown in Fig. 4.8. For a non-interacting system ($U = 0$) $\langle n_{\uparrow}n_{\downarrow} \rangle = 0.25$, and it gets lower with increasing interaction strength. In

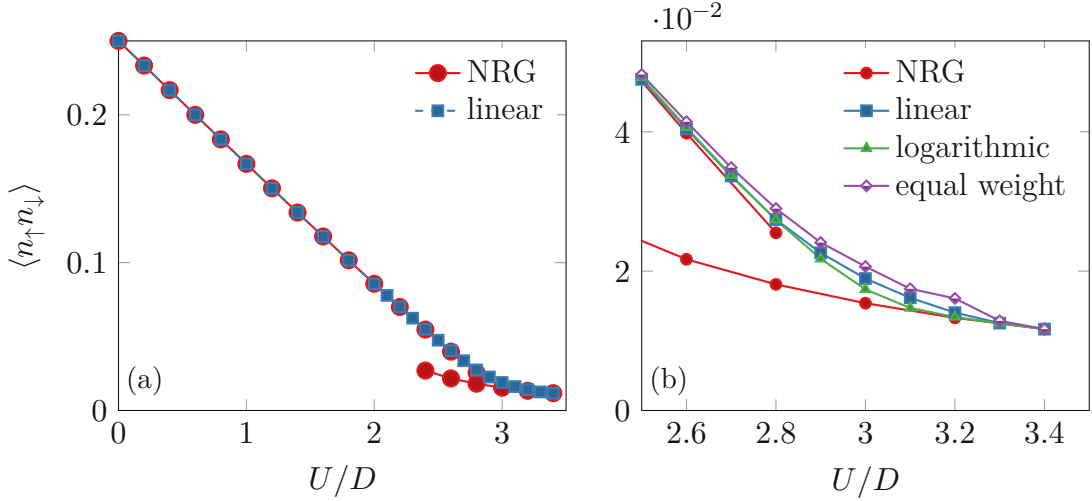


Figure 4.8.: Double occupation $\langle n_{\uparrow}n_{\downarrow} \rangle$ on the ground state as a function of U . The discretization of the hybridization function was varied between methods. (a) Comparison against NRG data [57]. (b) Zoom-in close to the metal-insulator transition.

Fig. 4.8(a) we see that our solver has very good agreement with NRG data [57] for weak to intermediate interaction strengths. In Fig. 4.8(b) we look at the transition using different discretization schemes of the hybridization function. (The broadening of spectra is zero.) In the linear and logarithmic discretization, the poles $\{\epsilon_i\}$ of the hybridization function are at fixed locations. For the former they are equidistant, while in the latter they are apart at a constant ratio $\epsilon_{i+1}/\epsilon_i = \Lambda$. In the equal weight discretization, the weights $\{V_i\}$ are set to be equal [21] while pole locations vary between each DMFT step. We see that up until $U/D \approx 2.5$ the double occupation is independent of the discretization. However, the value U where it equals the insulating solution of NRG differs. The logarithmic discretization becomes insulating at a value $U_{c2}/D \approx 3.2$, while for the linear and equal weight discretization it is around $U_{c2}/D \approx 3.3$. All of these values somewhat overshoot the NRG value of $U_{c2}/D = 2.94$ [15].

Using our method, it was not possible to find a metastable insulating solution. For any value $U < U_{c2}$, the solution immediately jumped to a metallic one. Thus, we cannot make any statement about U_{c1} .

Another way to find the value of U_{c2} is to look at the quasiparticle weight Z and see where it vanishes, corresponding to a diverging quasiparticle mass $m^* \rightarrow \infty$. To obtain it, we use equation Eq. (3.45) which diverges for a pole located at zero. The

4. Results

problem is that our Green's functions are numerically always insulating, and the self-energy always contains this problematic pole. E.g., for $U = 1$, we have a pole

$$\frac{9.39 \cdot 10^{-10}}{\omega + i0^+ + 5.94 \cdot 10^{-9}} \quad (4.6)$$

which is not visible in the spectrum. However, if one tries to calculate the quasiparticle weight it results in

$$Z = \left(1 + \frac{9.39 \cdot 10^{-10}}{(5.94 \cdot 10^{-9})^2}\right)^{-1} = (2.67 \cdot 10^7)^{-1} \approx 0. \quad (4.7)$$

Hence, we have to neglect poles with weights $< 3 \cdot 10^{-5}$ in the calculation of Eq. (3.45). In Fig. 4.9(a) our quasiparticle weight is higher than the NRG data, similar to [46, 47] where a D-DMRG solver was used. In Fig. 4.9(b) we look at the transition

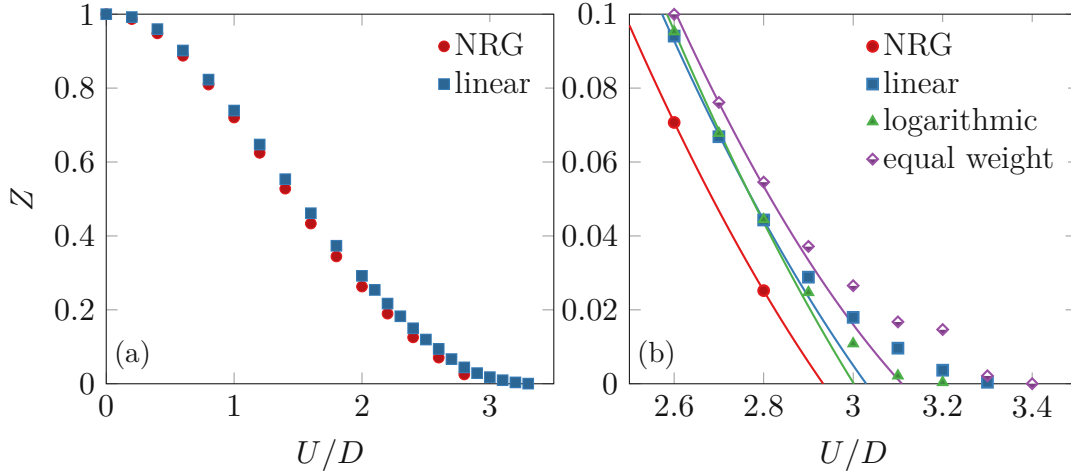


Figure 4.9.: Evolution of the quasiparticle weight Z with increasing interaction strength U . The discretization of the hybridization function was varied between methods. (a) Comparison against NRG data [57]. (b) Quasiparticle weight close to the metal-insulator transition. Lines are fits using data points $U/D \in [2, 2.8]$ [47].

using the same discretization schemes as in the double occupation. We see the same behavior: The logarithmic discretization becoming insulating first followed by the linear and equal weight discretization.

In [46, 47], computed data in the interval $U/D \in [2.0, 2.8]$ was used to fit a quadratic function

$$f_Z(U) = a_1(U - U_{c2}) + a_2(U - U_{c2})^2. \quad (4.8)$$

If we fit our data using the same interval, we get the lines shown in Fig. 4.9(b). Our logarithmic discretization now becomes metallic at $U_{c2}/D = 3$ closely followed by the linear discretization. The equal weight one becomes insulating at $U_{c2}/D = 3.1$. We

attribute this difference of the fit against the measured data points in $U/D \in (2.8, 3.4]$ as discretization artifacts stemming from the fact that we do not have enough poles close to the Fermi-level, in contrast to NRG.

4.7. $CeRu_4Sn_6$

Here, we briefly test our code for the material $CeRu_4Sn_6$ [58–60]. The Ce- f orbital is in a partially filled state giving rise to strong electronic correlations. We created a one-orbital Hubbard model with interaction strength $U = 5.5$ eV [59]. During the DMFT steps we used a Lorentzian broadening of $\delta = 0.04$ eV as the method of calculating the self-energy using the Schur complement (Eq. (3.41)) without broadening was not implemented at this time.

In Fig. 4.10 we plot the resulting spectral function which has the classical three-peak structure with lower and upper Hubbard bands and a central Kondo peak. As

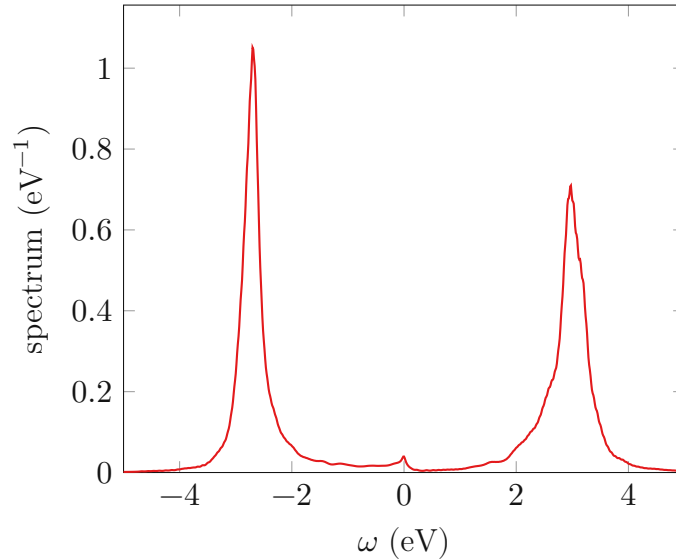


Figure 4.10.: DMFT impurity spectral function for the one-orbital model of $CeRu_4Sn_6$.

the system is not half-filled, the locations and structure of the Hubbard bands are not mirrors of each other. At zero temperature, the Kondo peak must be at the Fermi-level, which is the case for our calculation. However, due to the finite value of δ , its height is much smaller than anticipated. This may be improved by using the method with zero broadening instead.



Die approbierte gedruckte Originalversion dieser Diplomarbeit ist an der TU Wien Bibliothek verfügbar
The approved original version of this thesis is available in print at TU Wien Bibliothek.

5. Conclusion and outlook

In this thesis we developed and implemented a DMFT impurity solver which works on the real axis at zero temperature. By utilizing the natural impurity orbitals and restricted active space approach [20, 21], we successfully transform our problem from an exponentially scaling one to a polynomial one. While previously a few number of bath sites was the limiting factor for ED, this approach allows us to couple the impurity to hundreds of bath sites. To calculate the self-energy, we use the *symmetric improved estimator* [25] without any broadening using the Schur complement.

We then tested the code on the half-filled Bethe lattice in infinite dimensions. By continuously increasing the Coulomb interaction U , we obtain a critical value $U_{c2}/D \in [3.0, 3.3]$ for the Mott metal-to-insulator transition. The exact value depends on the discretization of the hybridization function and method used to extract U_{c2} . For intermediate interaction strength, the pinning condition $\pi DA(\omega = 0) = 2.0$ is well fulfilled. We observe small peaks at the inner edge of the Hubbard bands, comparable to previous results [46, 47, 61]. To obtain the quasi-particle weight Z , we can directly use the derivative of the real part of the self-energy without taking a finite difference quotient. Comparison of the low order moments of the Green's function and self-energy show excellent agreement against analytical results.

The solver was then briefly tested on a one-orbital model of CeRu_4Sn_6 . As a finite broadening was used, the height of the Kondo peak was smaller than anticipated. It may be possible to improve this calculation by using the approach based on the Schur complement.

There are multiple directions to improve and enhance the current code: First, it was not possible to find a metastable insulating solution. A variety of approaches were unsuccessfully tested: mixing of the self-energy between steps with a parameter α as low as 0.01; using a Hubbard-III approximation for the initial hybridization function; starting with an insulating self-energy with all weight concentrated at a single pole at the Fermi-level.

Second, multithreading performance can be improved. Currently, using lots of cores improves the speed-up by a factor of less than two. Applying the Hamiltonian onto a wave function will linearly combine Slater determinants leading to memory conflict. Here, one must find a performant algorithm without race conditions.

Last, for realistic material calculations one needs to expand the code to multi-orbital systems. As this will further increase computational complexity, optimizations mentioned in the previous step should be done first.

The code discussed in this thesis is contained in two packages: `Fermions.jl` [37] (not yet public) and `RAS_DMFT.jl` (https://github.com/frankebel/RAS_DMFT.jl).



Die approbierte gedruckte Originalversion dieser Diplomarbeit ist an der TU Wien Bibliothek verfügbar
The approved original version of this thesis is available in print at TU Wien Bibliothek.

A. Derivations

A.1. Fourier transform of the retarded correlator

In this section we perform the Fourier transform of the retarded correlator given in Eq. (2.12), and show how to arrive at Eq. (2.14). As the transformation is linear, we can transform each term separately:

$$C_\omega = \lim_{\delta \rightarrow 0^+} -i \int_0^\infty dt e^{i(\omega+i\delta)t} \langle A(t)B \rangle + \langle BA(t) \rangle \quad (\text{A.1})$$

$$= \lim_{\delta \rightarrow 0^+} -i \int_0^\infty dt e^{i(\omega+i\delta)t} \langle A(t)B \rangle + \lim_{\delta \rightarrow 0^+} -i \int_0^\infty dt e^{i(\omega+i\delta)t} \langle BA(t) \rangle \quad (\text{A.2})$$

$$= C_\omega^+ + C_\omega^- \quad (\text{A.3})$$

We define the complex frequency $z = \omega + i\delta$ and take the limit $\delta \rightarrow 0^+$ at the end. Transformation of the first component:

$$C_z^+ = -i \int_0^\infty dt e^{izt} \langle e^{iHt} A e^{-iHt} B \rangle \quad (\text{A.4})$$

$$= -i \int_0^\infty dt e^{izt} \langle e^{iE_0 t} A e^{-iHt} B \rangle \quad (\text{A.5})$$

$$= -i \int_0^\infty dt \langle A e^{i(z-H+E_0)t} B \rangle \quad (\text{A.6})$$

$$= -i \left\langle A \frac{e^{i(z-H+E_0)t}}{i(z-H+E_0)} B \right\rangle \Big|_0^\infty \quad (\text{A.7})$$

$$= -i \left(0 - \left\langle A \frac{1}{i(z-H+E_0)} B \right\rangle \right) \quad (\text{A.8})$$

$$= \left\langle A \frac{1}{z-(H-E_0)} B \right\rangle \quad (\text{A.9})$$

Taking the limit gives

$$C_\omega^+ = \lim_{\delta \rightarrow 0^+} \left\langle A \frac{1}{z-(H-E_0)} B \right\rangle = \left\langle A \frac{1}{\omega + i0^+ - (H-E_0)} B \right\rangle. \quad (\text{A.10})$$

A. Derivations

Transformation of the second component:

$$C_z^- = -i \int_0^\infty dt e^{izt} \langle B e^{iHt} A e^{-iHt} \rangle \quad (\text{A.11})$$

$$= -i \int_0^\infty dt e^{izt} \langle B e^{iHt} A e^{-iE_0 t} \rangle \quad (\text{A.12})$$

$$= -i \int_0^\infty dt \langle B e^{i(z+H-E_0)t} A \rangle \quad (\text{A.13})$$

$$= \left\langle B \frac{1}{z + (H - E_0)} A \right\rangle. \quad (\text{A.14})$$

Taking the limit gives

$$C_\omega^- = \lim_{\delta \rightarrow 0^+} \left\langle A \frac{1}{z + (H - E_0)} B \right\rangle = \left\langle A \frac{1}{\omega + i0^+ + (H - E_0)} B \right\rangle. \quad (\text{A.15})$$

A.2. DMFT simplification

We show how the calculation of the (local) lattice Green's function can be skipped in infinite dimensions. Instead, the hybridization function is directly obtained from a given self-energy. To emphasize function arguments, we will forego the compact notation with parameters as subscripts and write them in brackets instead, e.g., $G_\omega \rightarrow G(\omega)$.

In the limit of infinite dimensions, the self-energy is \mathbf{k} -independent and the lattice Green's function can be evaluated from its non-interacting counterpart

$$G_0(\mathbf{k}, \omega) = \frac{1}{\omega + i0^+ + \mu_0 - \epsilon(\mathbf{k})} \quad (\text{A.16})$$

$$G(\mathbf{k}, \omega) = \frac{1}{\omega + i0^+ + \mu - \epsilon(\mathbf{k}) - \Sigma(\omega)} \quad (\text{A.17})$$

$$= G_0(\mathbf{k}, \omega + \mu - \mu_0 - \Sigma(\omega)). \quad (\text{A.18})$$

The same holds for the lattice Green's function which is just the average over the Brillouin zone

$$G_{\text{loc}}(\omega) = G_{\text{loc},0}(\omega + \mu - \mu_0 - \Sigma(\omega)). \quad (\text{A.19})$$

We then map this lattice problem onto our impurity Green's function $G(\omega)$. Without a Coulomb interaction on the lattice this requires

$$[\mathcal{G}_0(\omega)]^{-1} = [G_{\text{loc},0}(\omega)]^{-1} \quad (\text{A.20})$$

$$= \omega + i0^+ + \mu_0 - \epsilon - \Delta_0(\omega), \quad (\text{A.21})$$

whereas in the interacting case it can be written as

$$[\mathcal{G}_0(\omega)]^{-1} = [G_{\text{loc}}(\omega)]^{-1} + \Sigma(\omega) \quad (\text{A.22})$$

$$= [G_{\text{loc},0}(\omega + \mu - \mu_0 - \Sigma(\omega))]^{-1} + \Sigma(\omega) \quad (\text{A.23})$$

$$= \omega + i0^+ + \mu - \epsilon - \Delta_0(\omega + \mu - \mu_0 - \Sigma(\omega)) \quad (\text{A.24})$$

$$\equiv \omega + i0^+ + \mu - \epsilon - \Delta(\omega). \quad (\text{A.25})$$

Comparing the last two lines, we can immediately deduce

$$\Delta(\omega) = \Delta_0(\omega + \mu - \mu_0 - \Sigma(\omega)). \quad (\text{A.26})$$

A.3. Shifting of poles

We want to set arbitrary poles onto an initially defined grid while conserving the zeroth and first moment locally. A single pole can be written as

$$\frac{w}{\omega + i0^+ - \epsilon}, \quad (\text{A.27})$$

with location $\epsilon \notin \{\epsilon_i\}$ not being part of our sorted list of grid points. To merge the point, we find the closest pole location such that $\epsilon_i < \epsilon < \epsilon_{i+1}$. Conserving the moments enforces

$$w = w_i + w_{i+1}, \quad (\text{A.28})$$

$$w\epsilon = w_i\epsilon_i + w_{i+1}\epsilon_{i+1}. \quad (\text{A.29})$$

Rearranging gives

$$w_i = w \frac{\epsilon - \epsilon_i}{\epsilon_{i+1} - \epsilon_i}, \quad (\text{A.30})$$

$$w_{i+1} = w \frac{\epsilon_{i+1} - \epsilon}{\epsilon_{i+1} - \epsilon_i}. \quad (\text{A.31})$$

If the pole is outside our interval such that $\epsilon < \epsilon_1$ or $\epsilon_N < \epsilon$, we shift the pole and weight to the first or last location respectively. This conserves the zeroth moment, while violating the first one. In practice, our interval is large enough such that poles where this occurs have weight of the order $O(\epsilon_{\text{MP}})$ posing no practical issue.

A.4. Number of Slater determinants

We derive an analytic expression which allows us to calculate the number of Slater determinants which constitute to our wave function for a set of given parameters. In the following we will use capital letters for the number of sites and lower case for their filling, e.g., $n = 10$ electrons distributed equally ($n_\uparrow = n_\downarrow = 5$) on $N = 9$ bath sites would generate

$$\binom{1+N}{n_\uparrow} \binom{1+N}{n_\downarrow} = \binom{10}{5} \binom{10}{5} = 63\,504 \quad (\text{A.32})$$

A. Derivations

states (we add one site for the impurity). As our Hamiltonian is $SU(2)$ symmetric, we can look at the spin-up and spin-down blocks separately.

For a choice L we have $N_I = 2 + 2L$ sites to be treated exactly in $|\psi_I\rangle$ (one impurity, one mirror site, and L valence and conduction sites respectively). This sets the number of Slater determinants to

$$\binom{N_I}{n_{I\uparrow}} \binom{N_I}{n_{I\downarrow}}, \quad (\text{A.33})$$

with $n_{I\uparrow} = n_{I\downarrow} = N_I/2$ for half-filling. This leaves $N_{II} = N - 1 - 2L$ sites inside the remaining chains $|\psi_{II}\rangle$ which can be further split into N_{IIv} valence sites and N_{IIc} conduction sites. (At half-filling we have $N_{IIv} = N_{IIc} = N_{II}/2$.) For $p = 0$ these partial chains are fully filled and fully empty respectively, limiting our partial wave function to

$$|\psi_{II}\rangle = |\mathbb{1}_v\rangle \otimes |0_c\rangle.$$

This constitutes one Slater determinant written as

$$\binom{N_{IIv}}{n_{IIv\uparrow}} \binom{N_{IIc}}{n_{IIc\uparrow}} \binom{N_{IIv}}{n_{IIv\downarrow}} \binom{N_{IIc}}{n_{IIc\downarrow}} = \binom{N_{IIv}}{N_{IIv}} \binom{N_{IIc}}{0} \binom{N_{IIv}}{N_{IIv}} \binom{N_{IIc}}{0} = 1. \quad (\text{A.34})$$

For the total number of states we then multiply Eqs. (A.33) and (A.34) together,

$$N_{p=0} = \binom{N_I}{n_{I\uparrow}} \binom{N_I}{n_{I\downarrow}}. \quad (\text{A.35})$$

By setting $p = 1$, we generate additional states

$$N_{p=1} = \binom{N_I}{n_{I\uparrow} - 1} \binom{N_{IIv}}{N_{IIv}} \binom{N_{IIc}}{1} \binom{N_I}{n_{I\downarrow}} \binom{N_{IIv}}{N_{IIv}} \binom{N_{IIc}}{0} \quad (\text{A.36a})$$

$$+ \binom{N_I}{n_{I\uparrow}} \binom{N_{IIv}}{N_{IIv}} \binom{N_{IIc}}{0} \binom{N_I}{n_{I\downarrow} - 1} \binom{N_{IIv}}{N_{IIv}} \binom{N_{IIc}}{1} \quad (\text{A.36b})$$

$$+ \binom{N_I}{n_{I\uparrow} + 1} \binom{N_{IIv}}{N_{IIv} - 1} \binom{N_{IIc}}{0} \binom{N_I}{n_{I\downarrow}} \binom{N_{IIv}}{N_{IIv}} \binom{N_{IIc}}{0} \quad (\text{A.36c})$$

$$+ \binom{N_I}{n_{I\uparrow}} \binom{N_{IIv}}{N_{IIv}} \binom{N_{IIc}}{0} \binom{N_I}{n_{I\downarrow} + 1} \binom{N_{IIv}}{N_{IIv} - 1} \binom{N_{IIc}}{0} \quad (\text{A.36d})$$

for one electron (Eqs. (A.36a) and (A.36b)) or hole (Eqs. (A.36c) and (A.36d)) excitation. Here, the first three binomial coefficients in each term count the number of spin-up electrons in the sectors $N_{I\uparrow}$, $N_{IIv\uparrow}$, $N_{IIc\uparrow}$ and the last three the number of spin-down electrons in $N_{I\downarrow}$, $N_{IIv\downarrow}$, $N_{IIc\downarrow}$.

For $p = 2$ we generate

$$N_{p=2} = \begin{pmatrix} N_I \\ n_{I\uparrow} - 2 \end{pmatrix} \begin{pmatrix} N_{IIv} \\ N_{IIv} \end{pmatrix} \begin{pmatrix} N_{IIc} \\ 2 \end{pmatrix} \begin{pmatrix} N_I \\ n_{I\downarrow} \end{pmatrix} \begin{pmatrix} N_{IIv} \\ N_{IIv} \end{pmatrix} \begin{pmatrix} N_{IIc} \\ 0 \end{pmatrix} \quad (\text{A.37a})$$

$$+ \begin{pmatrix} N_I \\ n_{I\uparrow} \end{pmatrix} \begin{pmatrix} N_{IIv} \\ N_{IIv} \end{pmatrix} \begin{pmatrix} N_{IIc} \\ 0 \end{pmatrix} \begin{pmatrix} N_I \\ n_{I\downarrow} - 2 \end{pmatrix} \begin{pmatrix} N_{IIv} \\ N_{IIv} \end{pmatrix} \begin{pmatrix} N_{IIc} \\ 2 \end{pmatrix} \quad (\text{A.37b})$$

$$+ \begin{pmatrix} N_I \\ n_{I\uparrow} - 1 \end{pmatrix} \begin{pmatrix} N_{IIv} \\ N_{IIv} \end{pmatrix} \begin{pmatrix} N_{IIc} \\ 1 \end{pmatrix} \begin{pmatrix} N_I \\ n_{I\downarrow} - 1 \end{pmatrix} \begin{pmatrix} N_{IIv} \\ N_{IIv} \end{pmatrix} \begin{pmatrix} N_{IIc} \\ 1 \end{pmatrix} \quad (\text{A.37c})$$

$$+ \begin{pmatrix} N_I \\ n_{I\uparrow} \end{pmatrix} \begin{pmatrix} N_{IIv} \\ N_{IIv} - 1 \end{pmatrix} \begin{pmatrix} N_{IIc} \\ 1 \end{pmatrix} \begin{pmatrix} N_I \\ n_{I\downarrow} \end{pmatrix} \begin{pmatrix} N_{IIv} \\ N_{IIv} \end{pmatrix} \begin{pmatrix} N_{IIc} \\ 0 \end{pmatrix} \quad (\text{A.37d})$$

$$+ \begin{pmatrix} N_I \\ n_{I\uparrow} \end{pmatrix} \begin{pmatrix} N_{IIcv} \\ N_{IIv} \end{pmatrix} \begin{pmatrix} N_{II} \\ 0 \end{pmatrix} \begin{pmatrix} N_I \\ n_{I\downarrow} \end{pmatrix} \begin{pmatrix} N_{IIv} \\ N_{IIv} - 1 \end{pmatrix} \begin{pmatrix} N_{IIc} \\ 1 \end{pmatrix} \quad (\text{A.37e})$$

$$+ \begin{pmatrix} N_I \\ n_{I\uparrow} + 1 \end{pmatrix} \begin{pmatrix} N_{IIv} \\ N_{IIv} - 1 \end{pmatrix} \begin{pmatrix} N_{IIc} \\ 0 \end{pmatrix} \begin{pmatrix} N_I \\ n_{I\downarrow} - 1 \end{pmatrix} \begin{pmatrix} N_{IIv} \\ N_{IIv} \end{pmatrix} \begin{pmatrix} N_{IIc} \\ 1 \end{pmatrix} \quad (\text{A.37f})$$

$$+ \begin{pmatrix} N_I \\ n_{I\uparrow} - 1 \end{pmatrix} \begin{pmatrix} N_{IIv} \\ N_{IIv} \end{pmatrix} \begin{pmatrix} N_{IIc} \\ 1 \end{pmatrix} \begin{pmatrix} N_I \\ n_{I\downarrow} + 1 \end{pmatrix} \begin{pmatrix} N_{IIv} \\ N_{IIv} - 1 \end{pmatrix} \begin{pmatrix} N_{IIc} \\ 0 \end{pmatrix} \quad (\text{A.37g})$$

$$+ \begin{pmatrix} N_I \\ n_{I\uparrow} + 2 \end{pmatrix} \begin{pmatrix} N_{IIv} \\ N_{IIv} - 2 \end{pmatrix} \begin{pmatrix} N_{IIcv} \\ 0 \end{pmatrix} \begin{pmatrix} N_I \\ n_{I\downarrow} \end{pmatrix} \begin{pmatrix} N_{IIv} \\ N_{IIv} \end{pmatrix} \begin{pmatrix} N_{IIc} \\ 0 \end{pmatrix} \quad (\text{A.37h})$$

$$+ \begin{pmatrix} N_I \\ n_{I\uparrow} \end{pmatrix} \begin{pmatrix} N_{IIv} \\ N_{IIv} \end{pmatrix} \begin{pmatrix} N_{IIc} \\ 0 \end{pmatrix} \begin{pmatrix} N_I \\ n_{I\downarrow} + 2 \end{pmatrix} \begin{pmatrix} N_{IIv} \\ N_{IIv} - 2 \end{pmatrix} \begin{pmatrix} N_{IIc} \\ 0 \end{pmatrix} \quad (\text{A.37i})$$

$$+ \begin{pmatrix} N_I \\ n_{I\uparrow} + 1 \end{pmatrix} \begin{pmatrix} N_{IIv} \\ N_{IIv} - 1 \end{pmatrix} \begin{pmatrix} N_{IIc} \\ 0 \end{pmatrix} \begin{pmatrix} N_I \\ n_{I\downarrow} + 1 \end{pmatrix} \begin{pmatrix} N_{IIv} \\ N_{IIv} - 1 \end{pmatrix} \begin{pmatrix} N_{IIc} \\ 0 \end{pmatrix}. \quad (\text{A.37j})$$

accounting for electron-electron (Eqs. (A.37a) to (A.37c)), electron-hole (Eqs. (A.37d) to (A.37g)), and hole-hole (Eqs. (A.37h) to (A.37j)) excitations. This scheme can be continued to higher order $p \geq 3$ (not done here).

For our calculations which use $N = 301$ bath sites, we list the number of Slater determinants in Tab. A.1. Due to symmetry, the Hilbert space with one particle more has the same dimension as the one with one particle less. We observe that an increase of L by one unit increases the number of determinants by a factor of 12 to 14 as mentioned in the main work.

A. Derivations

Table A.1.: Number of Slater determinants for $N = 301$ bath sites and choice L, p . The half-filled block is used to calculate the ground state; The space with one particle more/less is used to obtain correlators.

L	p	half-filled	half-filled ± 1 particle
0	1	1 204	902
1	1	14 340	11 050
2	1	178 000	143 860
3	1	2 309 860	1 934 324
4	1	30 968 784	26 616 744
0	2	271 204	203 252
1	2	3 298 300	2 672 786
2	2	42 636 240	35 810 380
3	2	569 272 396	490 256 564
4	2	7 778 775 312	6 826 790 124

B. Code Tutorial

Here, we show the tutorial of the package `RAS_DMFT.jl` version 0.10.0. An up-to-date guide is available in the package documentation.

B.1. Non-interacting Bethe lattice in infinite dimensions

The non-interacting density is the Wigner semicircle distribution

$$\rho(\omega) = \frac{2}{\pi D^2} \sqrt{D^2 - \omega^2} \quad (\text{B.1})$$

from which we can define a non-interacting Green's function $G(\omega)$ with the relation

$$\rho(\omega) = -\frac{1}{\pi} \text{Im} G(\omega). \quad (\text{B.2})$$

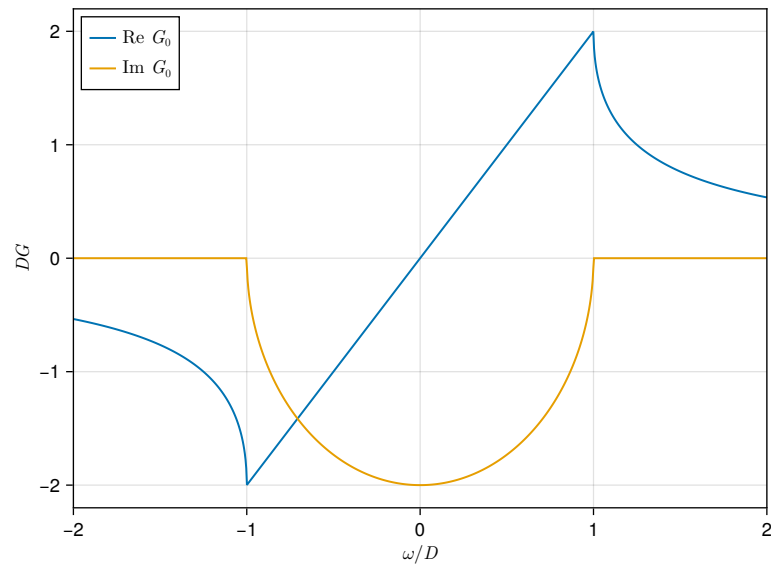
Let us plot it:

```

D = 1.0 # half-bandwidth
W = range(-2 * D, 2 * D; length = 1_000) # frequency grid
g = greens_function_bethe_analytic(W, D)

f = Figure();
ax = Axis(f[1, 1]; xlabel = L"\omega/D", ylabel = L"DG")
lines!(ax, W, real(g); label = L"\mathrm{Re}\sim G_0")
lines!(ax, W, imag(g); label = L"\mathrm{Im}\sim G_0")
axislegend(ax; position = :lt)
xlims!(ax, first(W), last(W))
  
```

B. Code Tutorial

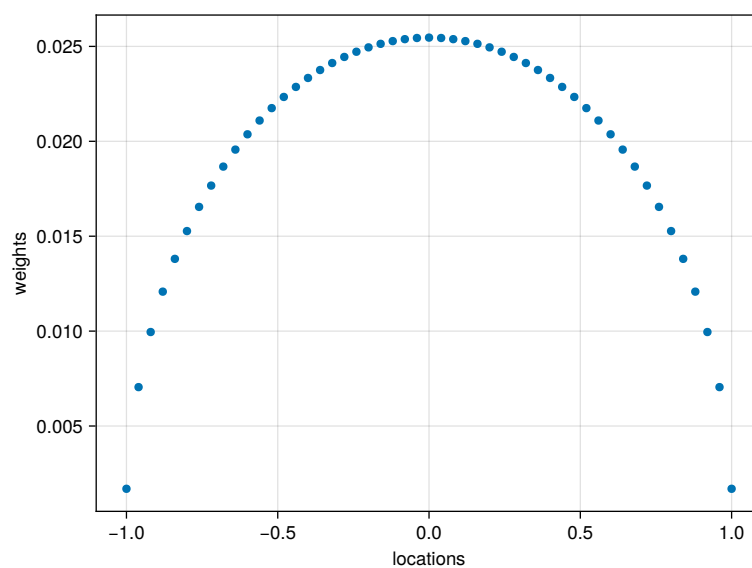


For calculations, we need to discretize this to N points:

```
N = 51 # number of points
grid = range(-D, D; length = N) # linear grid (others are possible)
G0 = greens_function_bethe_grid(grid)
```

This returns a PoleSum instance which only stores locations ϵ_i and weights w_i .

```
f = Figure();
ax = Axis(f[1, 1]; xlabel = "locations", ylabel = "weights")
plot!(ax, locations(G0), weights(G0))
```



B.1. Non-interacting Bethe lattice in infinite dimensions

We can see that this looks like a discrete version of our semicircle. Our spectrum is now

$$A(\omega) = \sum_i w_i \delta(\omega - \epsilon_i). \quad (\text{B.3})$$

If we introduce some broadening, this should look like the continuous one. Lorentzian broadening is characterized by δ

$$A(\omega) = \sum_i w_i \frac{1}{\pi} \frac{\delta}{(\omega - \epsilon_i)^2 + \delta^2}, \quad (\text{B.4})$$

Gaussian one by σ

$$A(\omega) = \sum_i w_i \frac{1}{\sqrt{2\pi\sigma^2}} \exp\left(-\frac{(\omega - \epsilon_i)^2}{2\sigma^2}\right). \quad (\text{B.5})$$

$\delta = \sigma = 0.04$

`f = Figure();`

`ax = Axis(f[1, 1]; xlabel = L"ω/D", ylabel = L"πDA(ω)")`

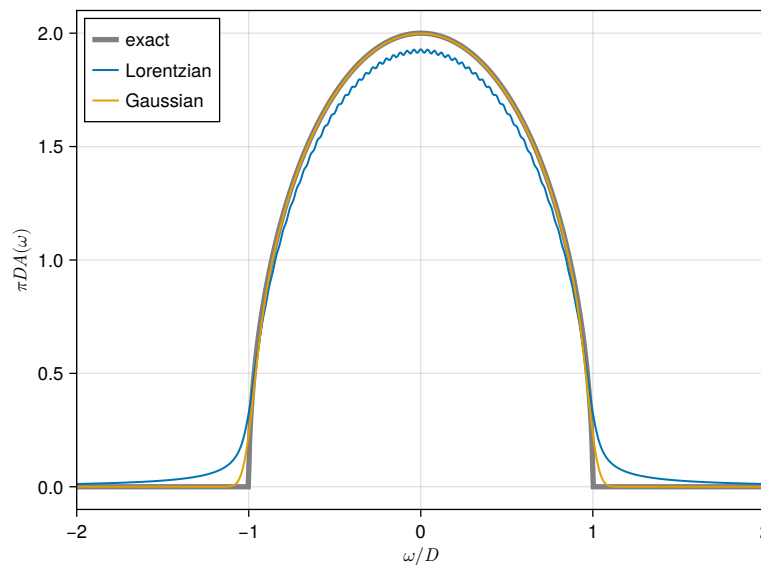
`lines!(ax, W, -imag(g); label = "exact", color = :gray, linewidth = 4)`

`lines!(ax, W, -imag(evaluate_lorentzian(G0, W, δ)); label = "Lorentzian")`

`lines!(ax, W, -imag(evaluate_gaussian(G0, W, σ)); label = "Gaussian")`

`axislegend(ax; position = :lt)`

`xlims!(ax, first(W), last(W))`



B.2. DMFT step

For all following calculations we set our unit of energy to $D = 1$.

B.2.1. Impurity

Values for the half-filled impurity. A value of $U/D = 2.0$ will generate a strongly correlated metal.

```
U = 2.0 # Coulomb interaction
μ = U / 2 # chemical potential
ε_imp = -μ # energy level for half-filling
# Restrictions for our active space.
L = 1 # number of chain sites to be treated exactly
p = 2 # order of excitations for remaining chains
```

Operators for exact part. This is necessary to introduce the interacting part and Hartree term. One can also introduce other operators, e.g., S_z , S^2 and measure their expectation values.

```
fs = FockSpace(Orbitals(2 + 2 * L), FermionicSpin(1 // 2))
c = annihilators(fs)
n = occupations(fs)
H_int = U * n[1, 1 // 2] * n[1, -1 // 2] # interacting Hamiltonian
d_dag = c[1, -1 // 2]' # d_↓^†
q_dag = H_int * d_dag - d_dag * H_int # auxiliary operator q_↓^† = [H_int, d^†]
# measure these on ground state
O_Σ_H = q_dag' * d_dag + d_dag * q_dag' # Operator for Hartree term
d_occ = n[1, 1 // 2] * n[1, -1 // 2] # double occupation
```

B.2.2. Hybridization function

On the Bethe lattice, the hybridization function Δ is nothing more than a rescaled Green's function

$$\Delta(\omega) = \frac{D^2}{4}G(\omega). \quad (\text{B.6})$$

We can create one using

```
n_bath = 51 # number of bath sites
grid = range(-4 * D, 4 * D; length = N) # linear grid
Δ0 = hybridization_function_bethe_grid(grid)
remove_zero_weight!(Δ0)
```

Here, we set our grid to $[-4D, 4D]$. This will initially create poles with zero weight. Due to the Coulomb interaction U , spectral weight will move to higher frequencies, such that poles with initially no weight will obtain a finite value in successive calculations.

B.2.3. Ground state

We can then calculate the ground state up to a user-given variance of the Hamiltonian $\text{Var}(H)$.

```
var = 1.0e-10
H, E0, ψ0 = init_system(Δ0, H_int, ε_imp, L, L, p, var);
# Given our ground state,
# we can calculate expectation values with `LinearAlgebra.dot`.
dot(ψ0, d_occ, ψ0) # expectation value
Σ_H = dot(ψ0, O_Σ_H, ψ0) # Hartree term, should be U/2 = 1.0
```

B.2.4. Block correlator

Shift to create diagonal matrices later.

```
q_dag_tilde = q_dag - Σ_H * d_dag
O_plus = [q_dag_tilde, d_dag] # for C+
O_minus = map(adjoint, O_plus); # for C-
```

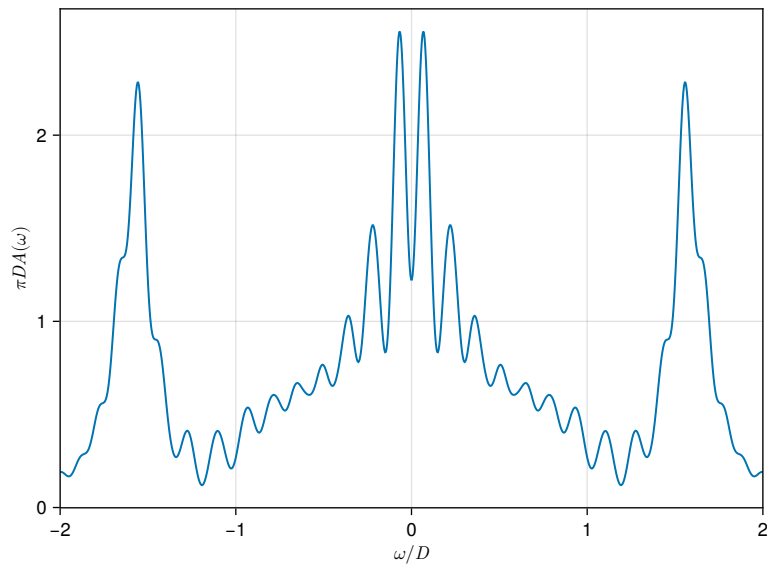
As we have two operators as input, we will create 2×2 block correlators. If we use n Krylov steps, each will have $2n$ poles.

```
n_kryl = 50
C_plus = correlator_plus(H, ψ0, O_plus, n_kryl)
C_minus = correlator_minus(H, ψ0, O_minus, n_kryl)
C = transpose(C_minus) + C_plus
```

We can plot the spectrum. The Green's function is the $[2, 2]$ component.

```
G = PolesSum(C, 2, 2)
f = Figure();
ax = Axis(f[1, 1]; xlabel = L"ω/D", ylabel = L"πDA(ω)")
lines!(ax, W, -imag(evaluate_gaussian(G, W, σ)))
xlims!(ax, first(W), last(W))
```

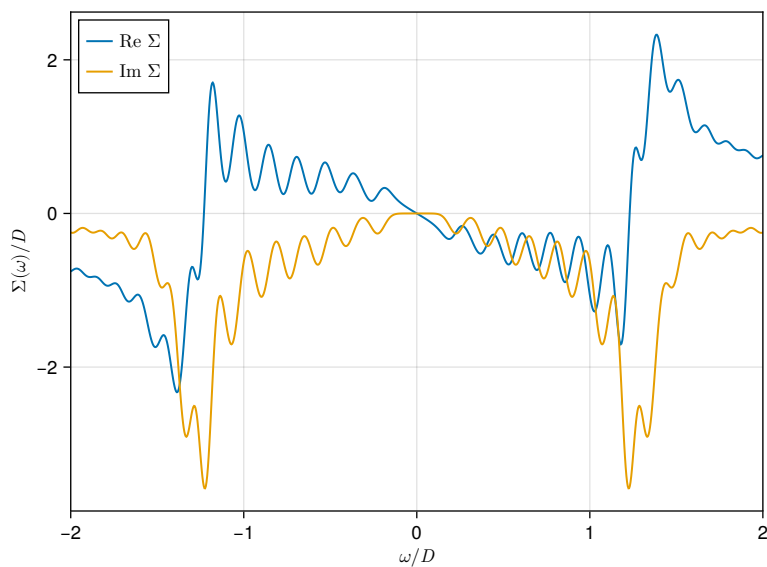
B. Code Tutorial



B.2.5. Self-energy

Here, we use the improved symmetric estimator [25] Σ^{IFG} .

```
\Sigma = self_energy_IFG(C)
sigma = evaluate_gaussian(\Sigma, W, \sigma)
f = Figure();
ax = Axis(f[1, 1]; xlabel = L"\omega/D", ylabel = L"\Sigma(\omega)/D")
lines!(ax, W, real(sigma); label = L"\mathrm{Re}\sim\Sigma")
lines!(ax, W, imag(sigma); label = L"\mathrm{Im}\sim\Sigma")
axislegend(ax; position = :lt)
xlims!(ax, first(W), last(W))
```



We can calculate the quasiparticle weight

$$Z = \left(1 - \frac{\partial \text{Re } \Sigma}{\partial \omega} \Big|_{\omega=0} \right)^{-1} \quad (\text{B.7})$$

$$= \left(1 + \sum_i \frac{w_i}{\epsilon_i^2} \right)^{-1} \quad (\text{B.8})$$

directly on the real axis without the use of a difference quotient. Due to poles at $\epsilon_i \approx 0$ this will diverge, and poles with small weight need to be ignored. This is controlled by the second parameter.

```
quasiparticle_weight( $\Sigma$ , sqrt(eps()))
```

B.2.6. Update hybridization

At the end of each DMFT step, we have to update the hybridization function using the new self-energy.

```
 $\Delta$  = update_hybridization_function( $\Delta_0$ ,  $\mu$ ,  $\Sigma_H$ ,  $\Sigma$ )
```

As this function has too many poles to be computationally feasible, we put them onto our initial grid

```
 $\Delta_{\text{grid}}$  = to_grid( $\Delta$ , grid)
```

We can then put this as our next input and continue at [App. B.2.3](#).



Die approbierte gedruckte Originalversion dieser Diplomarbeit ist an der TU Wien Bibliothek verfügbar
The approved original version of this thesis is available in print at TU Wien Bibliothek.

Bibliography

- [1] G. R. Stewart, “Heavy-fermion systems”, *Rev. Mod. Phys.* **56**, 755–787 (1984).
- [2] A. C. Hewson, *The Kondo problem to heavy fermions*, Cambridge Studies in Magnetism 2 (Cambridge University Press, Cambridge, 1993), 1 p.
- [3] D. Belitz and T. R. Kirkpatrick, “The Anderson-Mott transition”, *Rev. Mod. Phys.* **66**, 261–380 (1994).
- [4] M. Imada, A. Fujimori, and Y. Tokura, “Metal-insulator transitions”, *Rev. Mod. Phys.* **70**, 1039–1263 (1998).
- [5] R. M. Martin, L. Reining, and D. M. Ceperley, *Interacting electrons: theory and computational approaches* (Cambridge University Press, Cambridge, 2016).
- [6] W. Metzner and D. Vollhardt, “Correlated lattice fermions in $d = \infty$ dimensions”, *Phys. Rev. Lett.* **62**, 324–327 (1989).
- [7] A. Georges, G. Kotliar, W. Krauth, and M. J. Rozenberg, “Dynamical mean-field theory of strongly correlated fermion systems and the limit of infinite dimensions”, *Rev. Mod. Phys.* **68**, 13–125 (1996).
- [8] K. Held, “Electronic structure calculations using dynamical mean field theory”, *Adv. Phys.* **56**, 829–926 (2007).
- [9] J. E. Hirsch and R. M. Fye, “Monte Carlo method for magnetic impurities in metals”, *Phys. Rev. Lett.* **56**, 2521–2524 (1986).
- [10] E. Gull, A. J. Millis, A. I. Lichtenstein, A. N. Rubtsov, M. Troyer, and P. Werner, “Continuous-time Monte Carlo methods for quantum impurity models”, *Rev. Mod. Phys.* **83**, 349–404 (2011).
- [11] M. Wallerberger, “W2dynamics: continuous time quantum Monte Carlo calculations of one- and two-particle propagators”, PhD thesis (Technische Universität Wien, 2016).
- [12] M. Wallerberger, A. Hausoel, P. Gunacker, A. Kowalski, N. Parragh, F. Goth, K. Held, and G. Sangiovanni, “W2dynamics: local one- and two-particle quantities from dynamical mean field theory”, *Comput. Phys. Commun.* **235**, 388–399 (2019).
- [13] K. G. Wilson, “The renormalization group: critical phenomena and the Kondo problem”, *Rev. Mod. Phys.* **47**, 773–840 (1975).
- [14] R. Bulla, A. C. Hewson, and T. Pruschke, “Numerical renormalization group calculations for the self-energy of the impurity Anderson model”, *J. Phys.: Condens. Matter* **10**, 8365 (1998).

Bibliography

- [15] R. Bulla, “Zero temperature metal-insulator transition in the infinite dimensional Hubbard model”, *Phys. Rev. Lett.* **83**, 136–139 (1999).
- [16] R. Bulla, T. A. Costi, and T. Pruschke, “Numerical renormalization group method for quantum impurity systems”, *Rev. Mod. Phys.* **80**, 395–450 (2008).
- [17] J. Jaklič and P. Prelovšek, “Lanczos method for the calculation of finite-temperature quantities in correlated systems”, *Phys. Rev. B* **49**, 5065–5068 (1994).
- [18] M. Caffarel and W. Krauth, “Exact diagonalization approach to correlated fermions in infinite dimensions: Mott transition and superconductivity”, *Phys. Rev. Lett.* **72**, 1545–1548 (1994).
- [19] M. Capone, L. de’Medici, and A. Georges, “Solving the dynamical mean-field theory at very low temperatures using the Lanczos exact diagonalization”, *Phys. Rev. B* **76**, 245116 (2007).
- [20] Y. Lu, M. Höppner, O. Gunnarsson, and M. W. Haverkort, “Efficient real-frequency solver for dynamical mean-field theory”, *Phys. Rev. B* **90**, 085102 (2014).
- [21] Y. Lu, X. Cao, P. Hansmann, and M. W. Haverkort, “Natural-orbital impurity solver and projection approach for Green’s functions”, *Phys. Rev. B* **100**, 115134 (2019).
- [22] M. Jarrell and J. E. Gubernatis, “Bayesian inference and the analytic continuation of imaginary-time quantum Monte Carlo data”, *Phys. Rep.* **269**, 133–195 (1996).
- [23] K. S. D. Beach, R. J. Gooding, and F. Marsiglio, “Reliable Padé analytical continuation method based on a high-accuracy symbolic computation algorithm”, *Phys. Rev. B* **61**, 5147–5157 (2000).
- [24] J. Kaufmann and K. Held, “Ana_cont: Python package for analytic continuation”, *Comput. Phys. Commun.* **282**, 108519 (2023).
- [25] F. B. Kugler, “Improved estimator for numerical renormalization group calculations of the self-energy”, *Phys. Rev. B* **105**, 245132 (2022).
- [26] J. Kaufmann, P. Gunacker, A. Kowalski, G. Sangiovanni, and K. Held, “Symmetric improved estimators for continuous-time quantum Monte Carlo”, *Phys. Rev. B* **100**, 75119 (2019).
- [27] E. P. Wigner, “Characteristic vectors of bordered matrices with infinite dimensions”, *Ann. Math.* **62**, 548–564 (1955).
- [28] M. L. Mehta, *Random matrices*, Third edition, Pure and Applied Mathematics (Academic Press) 142 (Elsevier, Amsterdam, 2004), 688 pp.
- [29] M. Wallerberger, private communication, 2025.
- [30] M. Eckstein, M. Kollar, K. Byczuk, and D. Vollhardt, “Hopping on the Bethe lattice: exact results for densities of states and dynamical mean-field theory”, *Phys. Rev. B* **71**, 235119 (2005).

- [31] J. Hubbard and B. H. Flowers, “Electron correlations in narrow energy bands”, *Proc. R. Soc. Lond., A. Math. Phys. Sci.* **276**, 238–257 (1997).
- [32] P. W. Anderson, “Localized magnetic states in metals”, *Phys. Rev.* **124**, 41–53 (1961).
- [33] E. N. Economou, *Green’s functions in quantum physics*, Vol. 7, Springer Series in Solid-State Sciences (Springer, Berlin, Heidelberg, 2006).
- [34] M. Potthoff, T. Wegner, and W. Nolting, “Interpolating self-energy of the infinite-dimensional Hubbard model: modifying the iterative perturbation theory”, *Phys. Rev. B* **55**, 16132–16142 (1997).
- [35] A. Začinskis, “Benchmarking real-frequency dynamical mean-field theory and novel zero-broadening approach for calculating self-energy”, MA thesis (Heidelberg University, 2025).
- [36] M. Braß, “Ab initio calculations of the electron capture spectrum in ^{163}Ho ”, PhD thesis (Heidelberg University, Jan. 13, 2021).
- [37] M. Wallerberger and K. Held, “Trie-based ranking of quantum many-body states”, *Phys. Rev. Res.* **4**, 33238 (2022).
- [38] C. Lanczos, “An iteration method for the solution of the eigenvalue problem of linear differential and integral operators”, *J. Res. Natl. Bur. Stand.* **45**, 255 (1950).
- [39] C. C. Paige, “Computational variants of the Lanczos method for the eigenproblem”, *IMA J. Appl. Math.* **10**, 373–381 (1972).
- [40] C. C. Paige, “Error analysis of the Lanczos algorithm for tridiagonalizing a symmetric matrix”, *IMA J. Appl. Math.* **18**, 341–349 (1976).
- [41] J. Cullum and R. A. Willoughby, “A survey of Lanczos procedures for very large real ‘symmetric’ eigenvalue problems”, *J. Comput. Appl. Math.* **12–13**, 37–60 (1985).
- [42] G. H. Golub and C. F. Van Loan, *Matrix computations*, Fourth edition, Johns Hopkins Studies in the Mathematical Sciences (The Johns Hopkins University Press, Baltimore, 2013), 756 pp.
- [43] P.-O. Löwdin, “On the non-orthogonality problem connected with the use of atomic wave functions in the theory of molecules and crystals”, *J. Chem. Phys.* **18**, 365–375 (1950).
- [44] J. Schur, “Über Potenzreihen, die im Innern des Einheitskreises beschränkt sind”, *J. Reine Angew. Math.* **1917**, 205–232 (1917).
- [45] K. Ackermann, K. Arnold, M. Braß, C. Cardot, R. Green, S. Heinze, P. Hill, Y. Lu, S. Macke, M. Retegan, S. Shokri, M. Tagliavini, A. Zacinskis, and M. W. Haverkort, “QUANTY, a quantum many-body scripting toolkit”, (2024).
- [46] M. Karski, C. Raas, and G. S. Uhrig, “Electron spectra close to a metal-to-insulator transition”, *Phys. Rev. B* **72**, 113110 (2005).

Bibliography

- [47] M. Karski, C. Raas, and G. S. Uhrig, “Single-particle dynamics in the vicinity of the Mott-Hubbard metal-to-insulator transition”, *Phys. Rev. B* **77**, 75116 (2008).
- [48] J. Bezanson, A. Edelman, S. Karpinski, and V. B. Shah, “Julia: a fresh approach to numerical computing”, *SIAM Rev.* **59**, 65–98 (2017).
- [49] J. Chen and J. Revels, *Robust benchmarking in noisy environments*, arXiv.org, (Aug. 15, 2016) <https://arxiv.org/abs/1608.04295v1>.
- [50] R. Žitko and T. Pruschke, “Energy resolution and discretization artifacts in the numerical renormalization group”, *Phys. Rev. B* **79**, 85106 (2009).
- [51] E. Gull, D. R. Reichman, and A. J. Millis, “Bold-line diagrammatic Monte Carlo method: general formulation and application to expansion around the noncrossing approximation”, *Phys. Rev. B* **82**, 75109 (2010).
- [52] M. Granath and H. U. R. Strand, “Distributional exact diagonalization formalism for quantum impurity models”, *Phys. Rev. B* **86**, 115111 (2012).
- [53] M. Granath and J. Schött, “Signatures of coherent electronic quasiparticles in the paramagnetic Mott insulator”, *Phys. Rev. B* **90**, 235129 (2014).
- [54] M. Ganahl, P. Thunström, F. Verstraete, K. Held, and H. G. Evertz, “Chebyshev expansion for impurity models using matrix product states”, *Phys. Rev. B* **90**, 45144 (2014).
- [55] S.-S. B. Lee, J. von Delft, and A. Weichselbaum, “Doublon-holon origin of the subpeaks at the Hubbard band edges”, *Phys. Rev. Lett.* **119**, 236402 (2017).
- [56] S.-S. B. Lee and A. Weichselbaum, “Adaptive broadening to improve spectral resolution in the numerical renormalization group”, *Phys. Rev. B* **94**, 235127 (2016).
- [57] C. Gauvin-Ndiaye, J. Tindall, J. R. Moreno, and A. Georges, “Mott transition and volume law entanglement with neural quantum states”, *Phys. Rev. Lett.* **134**, 76502 (2025).
- [58] M. Sundermann, F. Strigari, T. Willers, H. Winkler, A. Prokofiev, J. M. Ablett, J.-P. Rueff, D. Schmitz, E. Weschke, M. M. Sala, A. Al-Zein, A. Tanaka, M. W. Haverkort, D. Kasinathan, L. H. Tjeng, S. Paschen, and A. Severing, “CeRu₄Sn₆: a strongly correlated material with nontrivial topology”, *Sci. Rep.* **5**, 17937 (2015).
- [59] P. Wissgott and K. Held, “Electronic structure of CeRu₄Sn₆: a density functional plus dynamical mean field theory study”, *Eur. Phys. J. B* **89**, 5 (2016).
- [60] J. Dobilas, M. Brass, F. T. Ebel, S. Paschen, and K. Held, *Weyl nodes in CeRu₄Sn₆ studied by dynamical mean-field theory*, (Aug. 26, 2025) <http://arxiv.org/abs/2507.12944>, pre-published.
- [61] M. Ganahl, M. Aichhorn, H. G. Evertz, P. Thunström, K. Held, and F. Verstraete, “Efficient DMFT impurity solver using real-time dynamics with matrix product states”, *Phys. Rev. B* **92**, 155132 (2015).